ABSTRACT

Title of Thesis: LOCOMOTION ON GRANULAR MEDIA: REDUCED-ORDER MODELS

Christina Nikiforidou
Master of Science, 2024

Thesis Directed by: Professor Balakumar Balachandran
Department of Mechanical Engineering

Deciphering and predicting the dynamics of locomotion over compliant terrain is garnering increasing interest because of its relevance to search and rescue missions, planetary explorations, as well as robot navigation on diverse surfaces. In the realm of assistive devices for individuals with limited ankle mobility, it is valuable for an assistive device to be of use in both indoor and outdoor environments. In this thesis research, the Dynamic Data-Driven Application Systems framework is employed and this framework is used to determine lower extremity trajectories for supporting the operation of a robotic device on uneven terrains. With this framework, data obtained from simulations is combined along with noisy sensor measurements to predict the contact forces of a leg interacting with granular media.

For the simulation of the dynamical responses of legged locomotion on granular media, two models are used. They are, namely, a reduced-order model based on the Resistive Forces Theory (RFT) and a high-fidelity model based on the Smoothed Particle Hydrodynamics (SPH) method. The results obtained with the two models are compared for various leg morphologies

to assess how well these models can be used to capture complex contact interactions between a robot appendage and granular media. After data collection from simulations, the efficiency of the proposed data-driven framework is illustrated and discussed by examining test cases that involve the gait responses of robotic appendages interacting with granular material. Preliminary experiments of foot interactions with granular media have also been conducted and this data has also been considered in the DDDAS framework.

The present work can serve as a basis for further developing the utility of the DDDAS framework for robot device operations, with a particular emphasis on assistive robots. The utility of data generated from off-line simulations and real-time data generated from sensors on these assistive robots can help the robots adapt better to different terrains.

LOCOMOTION ON GRANULAR MEDIA: REDUCED-ORDER MODELS

by

Christina Nikiforidou

Thesis submitted to the Faculty of the Graduate School of the
University of Maryland, College Park in partial fulfillment
of the requirements for the degree of
Master of Science
2024

Advisory Committee:

Professor Balakumar Balachandran, Mechanical Engineering, Chair and Advisor
Professor Peter W. Chung, Mechanical Engineering
Professor Teng Li, Mechanical Engineering

Dedication

To my sister and brother, who have been my source of inspiration and strength. Thank you for all your support along the way.

Acknowledgments

I would like to express my gratitude to my advisor, Professor Balakumar Balachandran, for granting me this opportunity for research and for his unwavering support and guidance throughout the entire duration of the project. His mentorship and breadth of knowledge served as a constant source of encouragement, particularly during challenging times.

I would also like to thank Dr. Anindo Roy, Doug Summerlin, and Nicholas Rabuck at NextStep Robotics for their assistance in discussing this work, and in particular their help in setting up the experiment for validating the reduced-order model.

I would like to extend my appreciation to the past and present members of the Dynamics and Controls lab, especially Dr. Guanjin Wang and Dr. Xiangxue Zhao, whose assistance and data helped support this research, as well as Dr. Shayak Bhattacharjee, whose valuable suggestions helped improve this thesis.

I am grateful to my committee members, Professor Peter Chung and Professor Teng Li, for agreeing to serve on my thesis committee and for the knowledge and insights gained from their classes, which contributed to my research endeavors.

Finally, the support received for this thesis work through the Maryland Industrial Partnerships Program (Award Number 306946-00001) and NextStep Robotics is gratefully acknowledged.

Table of Contents

List of Tables

List of Figures

Chapter 1: Introduction

In this chapter, motivation for the thesis work is provided, along with a brief literature review related to motion on granular media and a discussion of research goals and thesis organization.

1.1 Background and Motivation

Motion is ubiquitous, and by studying its origins and mechanisms over the years, scientists and engineers have developed theories and models that can be used to predict the complex behavior of machines that move, swim, and fly in natural environments. Recently, drawing inspiration from biological systems, especially legged animal locomotion, engineers have unlocked new capabilities in the field of robotics. Legged robots are anticipated to outperform wheeled robots on rough terrains in terms of speed and efficiency because of these robots' terrain adaptability, maneuverability, and obstacle negotiation capabilities [1]. As a result, the understanding and prediction of robot motions are garnering increasing interest. However, unlike the comprehensive modeling approaches available for describing the locomotion in continuous media such as Newtonian fluids (e.g., continuum models based on the Navier-Stokes equations), the modeling approaches available for predicting movement on terrestrial and granular surfaces are less well-established.

A terrestrial surface may consist of natural substrates such as sand, soil, and gravel that pose mobility challenges for autonomous machines. These granular substrates deform as they come into contact with a robot or the locomotor, resulting in complicated flows, forces, and reactions including sinkage and slip [2]. Other notable occurrences include the discontinuous flow of granular media, the formation of arches and bridges, and the development of frictional forces between particles [3]. These are all some distinguishing aspects of terrestrial locomotion and the interactions are nonlinear in nature. As a result of the complexity and nonlinearity of the interaction with granular media, physics, and mechanics alone may not be sufficient for the prediction of force reactions. Hence, intrusion into granular media remains a rheologically challenging phenomenon to model [4].

1.2 Literature Review

To date, various models and simulations have been employed to explore legged locomotion on granular media. A representative example is the Discrete Element Method (DEM), which is used to study granular media as an assembly of individual particles interacting with one another through contact mechanics. Maladen *et al.* [5] utilized DEM to study the locomotor dynamics of a lizard moving through sand. By incorporating the granular material properties as well as the leg design into their model, they estimated the particle-particle interactive forces and the resulting forces exerted on the intruding leg. Expanding upon this work, Qian *et al.* [6] leveraged the DEM computational model along with laboratory experiments to test how a lightweight hexapod robot can take advantage of the fluid-like properties of granular media to achieve high performance. Additionally, Ravula [7], [8] and Acar *et al.* [9] used DEM to study robot appendage interactions with granular media, particularly for robots on lugged wheels. In their work, they also performed experiments with photoelastic media to further examine the interactions of a lugged wheel and a pendulum with the media.

In addition to discrete-based approaches for modeling granular locomotion, there have been significant studies on continuum modeling of the associated dynamics. Notably, Wang *et al.* [10] established a computational model based on the Smoothed Particle Hydrodynamics (SPH) to simulate robotic appendage interactions with granular systems. Their approach enabled them to estimate interactive forces for a variety of robotic limb morphologies and they validated the results by comparing them to experimental findings obtained by Li *et al.* [11]. Furthermore, Wang *et al.* used the SPH based model to simulate the swinging motion of a robotic leg on granular media, offering insights into human-like gait over deformable terrain [12].

While both the DEM and SPH models can be used for granular locomotion modeling, they are computationally expensive. Li *et al.* [11], [13] proposed an empirical model based on the Resistive Forces Theory (RFT) to describe the interactions between a rigid robot limb and granular media. Their model can be used to quickly predict forces involved in legged locomotion on compliant terrains, and in particular, this model is suitable for cases where the intruding leg moves at slow speeds.

Despite the fact that several computational models have been developed for studying the dynamics of granular intrusion, the focus of each of these models mentioned above is on different aspects of the interactions. With RFT, for instance, one empirically evaluates the forces exerted on a rigid body moving within granular media while accounting for inter-particle contact forces and rearrangements. Conversely, with continuum-based models such as SPH, one focuses on macroscopic descriptions of granular materials and uses constitutive equations to describe the interactions.

1.3 Research Goals

In this research, one of the research goals of the author is to study and evaluate the empirical RFT model proposed by Li *et al.* [11] and compare the obtained force estimations with those obtained by using the SPH model, for different leg geometries interacting with granular media. This comparative analysis is an attempt to assess the validity of the two models in capturing the underlying interaction dynamics.

Additionally, no existing model has been previously used to obtain force estimations for human-sized robotic appendages interacting with granular media, an aspect that holds potential significance for the operation of assistive devices on compliant terrains. Current lower-extremity robotic devices are primarily designed for treadmill-based therapy, despite the majority of patients expressing a preference to exercise their gait on natural terrains that are often irregular and deformable. Addressing this need is another research goal of this thesis.

Given the computational intensity of SPH and DEM, the author of this thesis will leverage RFT to derive interactive forces between a human sized foot and granular material. The validation of these results involves preliminary experiments involving a dummy foot moving over granular media. These experiments were conducted in collaboration with NextStep Robotics, a startup company that is involved in designing a portable ankle robot (AMBLE) for patients with foot drop. With the approach used in this thesis, the aim is to explore the adaptability and performance of assistive robots across various terrains.

Within the scope of this thesis, another research goal is to explore the use of data-driven methods for examining robot-leg interactions with granular media. To address this research goal, the Dynamic Data-Driven Application Systems (DDDAS) paradigm is utilized to swiftly and accurately predict interactive forces during locomotion, facilitating decision-making for an assistive robot [14]. Originally introduced to address the growing need for adaptable data-driven models that can dynamically respond to changing conditions in real-time through data assimilation, with DDDAS, one integrates physics-based simulations and sensor measurements within a feedback control loop to make more well-informed predictions. In Fig. 1.1, a block diagram of the DDDAS paradigm is shown, as used by Zhao *et al.*, to predict the nonlinear aeroelastic responses of a joint wing [15], [16]. In the context of this thesis, data obtained by simulations conducted by using SPH and RFT models serve as the simulation data for granular intrusion of a leg, while experimental data are assimilated into DDDAS to continuously update force predictions in real-time.

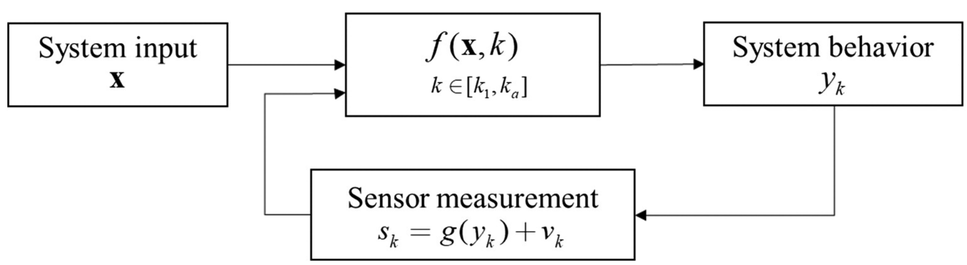

Figure 1.1: Representative block diagram of DDDAS [15].

1.4 Thesis Organization

The rest of the thesis is organized as follows. In Chapter 2, a reduced-order RFT model is developed for a variety of robot leg morphologies. The results are then compared to those obtained by using a SPH model. After validation, the author proceeds to estimate resistive forces for a human-sized foot traversing over granular media. In Chapter 3, the findings of preliminary experiments are presented as a way to validate the RFT force estimations for a human leg. In Chapter 4, data obtained from the SPH and RFT model based simulations are fed into the DDDAS for various test cases of robotic appendages interacting with granular material. Finally, in Chapter 5, the conclusions that can be drawn from this thesis work are presented and recommendations for future work are made. An appendix is included to provide the code developed for the RFT model based studies.

Chapter 2: Reduced-Order Models, Results, and Discussion

Legged locomotion offers unprecedented advantages for navigation on compliant terrain. In this chapter, the investigations and simulations conducted for various leg morphologies interacting with granular media are presented, to gain insights into the complexities of legged locomotion dynamics. Structured into three sections, this chapter is started with an overview of Smoothed Particle Hydrodynamics (SPH), and this overview is followed by an analysis of the development of the Resistive Forces Theory (RFT) computational framework. Finally, a comparison study based on the results obtained from the two models is presented.

2.1 Smoothed Particle Hydrodynamics

SPH is a physics-based continuum model, in which one uses a combination of the conservation laws of mass and momentum in fluid mechanics and the constitutive law in solid mechanics in order to simulate the flow of media. In their study, Wang *et al.* [10] developed an SPH based computational framework for modeling robot appendage interactions with a granular material, and this framework was validated by comparing the obtained results with experimental findings reported in the literature [11]. Through their work, they showed that a SPH methodology can be applied to understand interactions with granular media. A key idea underlying the SPH method is the fact that with this method, one discretizes the substrate domain into particles, wherein each particle has its own physical parameters such as mass, density, velocity, and pressure. These properties can then be interpolated across the neighboring particles to determine the desired parameter values at a given point by using a kernel function, $W(r, h)$, where r is the distance between particles and h is the smoothing length, which defines the interaction range.

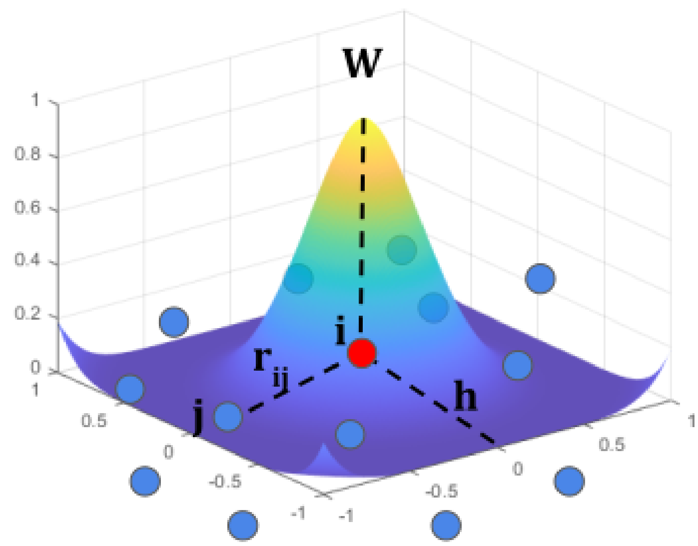

Figure 2.1: SPH is a mesh-free computational framework that is typically used to evaluate forces in viscous fluids and has also been proven to be useful for studying dynamics in granular media. By using different kernel functions (e.g., the Wendland Kernel function) for interpolation, the density and momentum at a specific particle position can be estimated.

In the SPH mathematical formulation (e.g., [10], [17], [18], [19]), the momentum equation is used to describe the movement of granular materials that experience external loads, whereas the continuity equation is used to describe the change in density of granular materials subjected to substantial deformation. The conservation of momentum equation reads as:

$$\frac{D\boldsymbol{v}}{Dt} = \frac{1}{\rho}(\nabla \cdot \boldsymbol{\sigma}) + \boldsymbol{b} \tag{2.1}$$

where $\boldsymbol{v}$ is the velocity vector, $\boldsymbol{\sigma}$ is the Cauchy stress tensor, ρ is the material density, and $\boldsymbol{b}$ is the body force (e.g., gravity), respectively. According to the conservation of mass equation, the rate of change of density is proportional to the negative of the divergence of the density times the velocity and is given by:

$$\frac{D\rho}{Dt} = -\nabla \cdot (\rho \boldsymbol{v}) \tag{2.2}$$

This equation is used to calculate the material density at a given time step. Then, the evaluation of density at a particle's position i can be achieved by using the kernel summation approach, written as [18]:

$$\frac{D\rho_i}{Dt} = \sum_j m_j (\boldsymbol{v_i} - \boldsymbol{v_j}) \cdot \boldsymbol{\nabla_i W_{ij}} \tag{2.3}$$

where m_j represents the mass of neighboring particle j, $(\boldsymbol{v_i} - \boldsymbol{v_j})$ denotes the velocity difference between particle i and particle j, and $\boldsymbol{\nabla_i W_{ij}}$ represents the gradient of a kernel function W_{ij} evaluated at the position of particle i with respect to the position of particle j.

The momentum equation, Eq. (2.1), can be approximated as [18]:

$$\frac{D\boldsymbol{v_i}}{Dt} = \sum_j m_j \left(\frac{\boldsymbol{\sigma_i}}{\rho_i^2} + \frac{\boldsymbol{\sigma_j}}{\rho_j^2} - \Pi_{ij} \right) \cdot \boldsymbol{\nabla_i W_{ij}} + \boldsymbol{b} \tag{2.4}$$

where $\frac{D\boldsymbol{v_i}}{Dt}$ represents the material derivative of the velocity of particle i with respect to time, $\boldsymbol{\sigma_i}$ and $\boldsymbol{\sigma_j}$ are the stress tensors of particles i and j, respectively, and Π_{ij} is the artificial viscosity employed for numerical stability.

Finally, with SPH, one can evaluate the forces acting on the leg interacting with granular media by employing the following equation [10]:

$$\boldsymbol{F} = \sum_{k \in robot} \sum_{j \in granular} m_k m_j \left(\frac{\boldsymbol{\sigma_i}}{\rho_i^2} + \frac{\boldsymbol{\sigma_j}}{\rho_j^2} - \Pi_{ij} \right) \cdot \boldsymbol{\nabla_i W_{ij}} \tag{2.5}$$

2.2 Resistive Forces Theory

RFT is a computational framework that was initially developed to quantitatively analyze the dynamics that occur when a slender body moves through a viscous fluid [20]. It has recently been demonstrated that the model can also capture terrestrial locomotion by shedding light on the resistive forces exerted on the locomotor's legs as they move through granular media [21]. Notably, when studying legged locomotion in a granular substrate, the heart of RFT lies in the concept that different parts of the leg may experience different resistive forces due to variations in the local conditions. This observation is highlighted in Fig. 2.2, which is used to illustrate the varying orientations, depths, and directions for different leg regions.

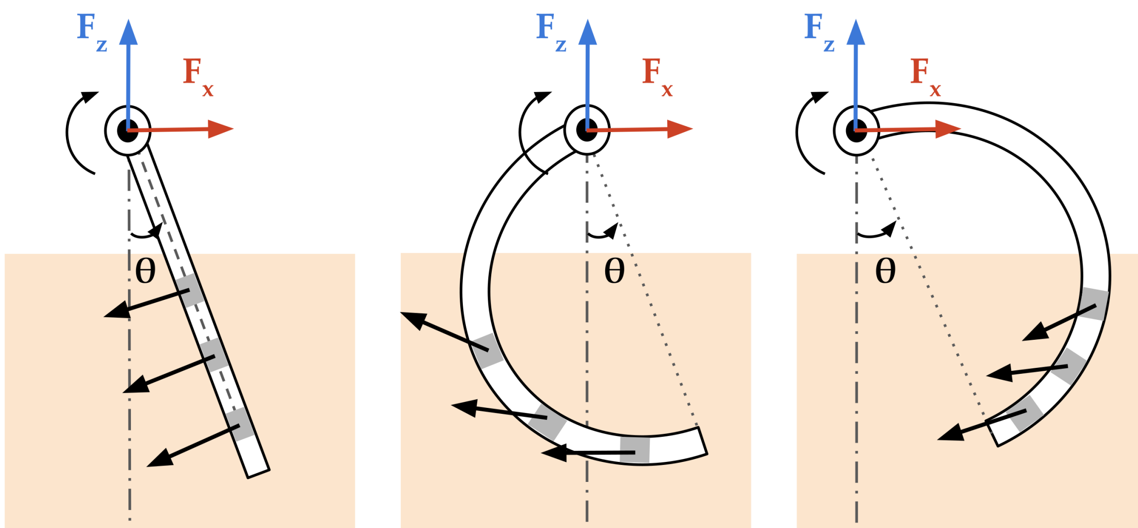

Figure 2.2: RFT model schematics for three different leg morphologies, a flat leg, a C-shaped leg, and a reverse C-shaped leg. The three legs revolve clockwise about an axis located at a certain hip height above the ground. Each leg is divided into numerous small sub-elements that have different orientations, depths, and directions of motion at a given time, as indicated by the plates and arrows. The net horizontal and vertical forces, F_x and F_z, can be estimated with linear superposition of all the element stress-generated forces.

In order to identify the individual resistive forces acting on separate parts of the leg, each leg is discretized into several small plate elements. Each plate element has its own unique geometric parameters that can be distinguished into the attack angle β, the intrusion angle γ, and the depth below the ground surface z. These parameters are illustrated for a single plate element in Fig. 2.3. The angle of attack is descriptive of the orientation of the element with respect to the horizontal plane, whereas the angle of intrusion is used to capture the velocity direction in which the element penetrates the granular material.

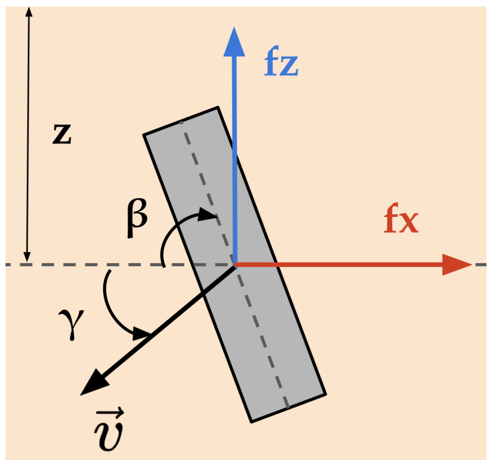

Figure 2.3: Illustration of the three parameters that element stress is dependent on. The depth z is the distance between the midpoint of the element and the surface of the granular media, the angle of attack β represents the orientation of the element plate, and the angle of intrusion γ represents the plate's direction of motion.

Taking the individual geometric parameters into account, and assuming that flowable media exhibits fluid-like properties when a plate submerges in it, according to RFT, the media exerts both vertical and horizontal hydrostatic-like stresses on each leg element. These resulting stresses can be expressed as follows:

$$\begin{cases} \sigma_z = \alpha_z(\beta, \gamma)|z| \\ \sigma_x = \alpha_x(\beta, \gamma)|z| \end{cases} \tag{2.6}$$

where α_z and α_x are the vertical and horizontal stresses per unit depth respectively.

Parameters α_z and α_x are extracted experimentally after conducting laboratory plate tests in granular media under various local conditions. In essence, one can use empirical RFT that is an extension of the theoretical framework, and for this, one incorporates real-world experimental measurements to capture the dynamic event's complexities. Even more specifically, the experimental parameters α_z and α_x are adopted from Li *et al.* [11]. In their work, it was observed that the granular stresses per unit depth are considerably affected by a submerged plate's orientation and direction of motion. This dependence of α_z and α_x on the attack angle β and intrusion angle γ is underscored in Fig. 2.4 in the form of contour plots.

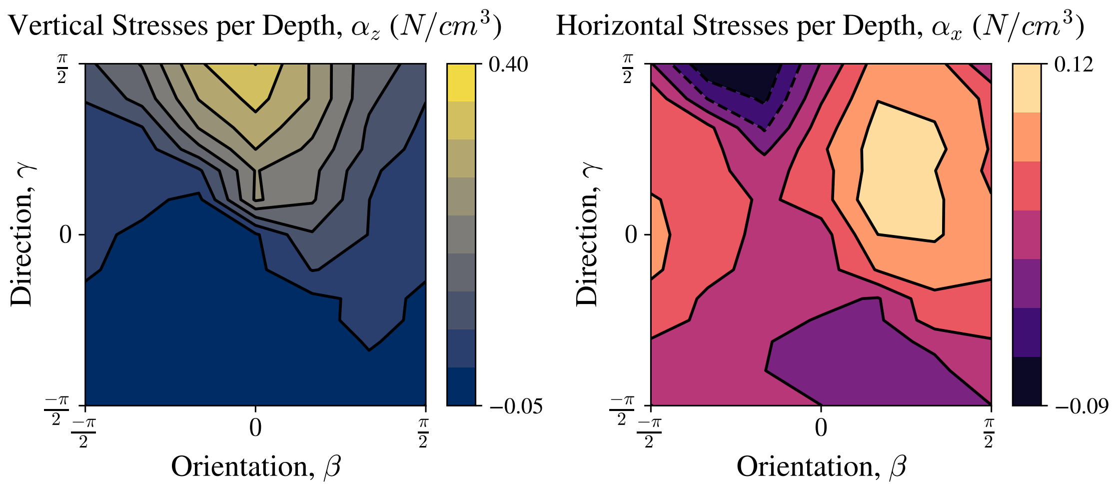

Figure 2.4: Distribution of horizontal and vertical stresses per unit depth, α_x and α_z, with respect to the angle of attack β and angle of intrusion γ. The color variation corresponds to the stress magnitude. The illustrated data were collected from experiments of plates moving through closely packed poppy seeds [11].

To evaluate the forces f_z and f_x acting on all intruder elements, each element stress is multiplied by the corresponding plate surface area; that is, $f_{z,x} = \sigma_{z,x}A$. In line with Li *et al.* [11], here, it is hypothesized that the net lift and drag forces can be predicted by applying the principle of linear superposition across all elements. Consequently, assuming that the intruder's leg is discretized into n elements, the net forces the leg experiences at a given time can be computed as follows:

$$\begin{cases} F_z = \sum_{i=1}^{n} \sigma_z(\beta_i, \gamma_i, |z|_i) A_i \\ F_x = \sum_{i=1}^{n} \sigma_x(\beta_i, \gamma_i, |z|_i) A_i \end{cases} \tag{2.7}$$

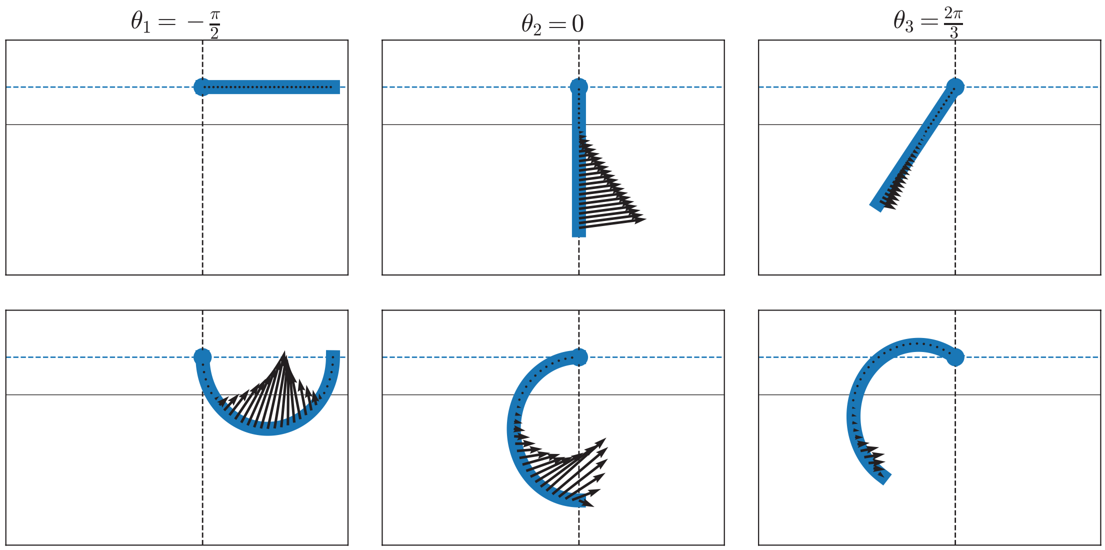

Figure 2.5: Sequence of frames that are used to depict the rotations of two leg shapes through granular media along with their element resistive forces at different time instants. The θ angle is negative during intrusion and positive during extraction.

In Fig. 2.5, a time-lapse of the dynamics that occur as two of the leg geometries rotate through granular media is presented. Each leg is divided into thirty elements and are placed at a hip height from the ground surface. As each leg is rotated, the leg elements interacting with the ground encounter resistive forces, which are represented by the black arrows on the leg profiles. The magnitude and direction of the element forces fluctuate as the depth and orientation of the elements change. The resistive forces are reported to be greater during intrusion for both leg morphologies, revealing that it takes more effort to propel the leg into granular media than to withdraw it. Overall, the element resistive forces offer considerable insight into the net lift and drag $F_{z,x}$, which can be determined by linear superposition of all force vectors' vertical and horizontal components at a given time instant.

2.2.1 Data Pre-Processing

In this study, an empirical RFT model is employed, thus utilizing experimental data gathered by Li *et al.* [11]. The data corresponds to the horizontal and vertical resistive forces that a leg experiences at a given depth from the granular surface. During the experiments, a flat-leg element is gradually submerged in various granular media, spanning different orientations and directions. Then, the resulting resistive forces per unit depth were derived for a range of β and γ angles, as depicted in Fig. 2.4, which is from an experiment conducted with a granular media bed containing loosely packed poppy seeds.

These surface plots can inform one about the underlying trends in the dataset. Specifically, it is evident that normal stresses reach their maximum values when the leg element has a zero attack angle and a positive angle of intrusion. From this observation, one can infer that there is a greater normal resistance when a leg element is intruding into the granular media compared to when it is being extracted. Interestingly, during the extraction phase, characterized by negative gamma angles, the normal stresses approach zero for nearly the entire range of beta values.

Similarly, the longitudinal stresses are found to peak when the gamma angle is zero and there is a positive angle of attack. This observation suggests that the maximum longitudinal resistance occurs under conditions where the leg element is oriented perpendicularly to the surface of the granular media and is penetrating it at an optimal angle.

Due to the limitation of the β and γ angle values for which force measurements are available, it is crucial to implement interpolation techniques to fill in the missing data.

Interpolation serves as a method to bridge the discrete dataset, allowing for the estimation of values at intermediate grid points lying between the provided data points. This approach facilitates the transition from a discrete to a more continuous distribution of data points, enabling a more flexible and informative framework for analysis.

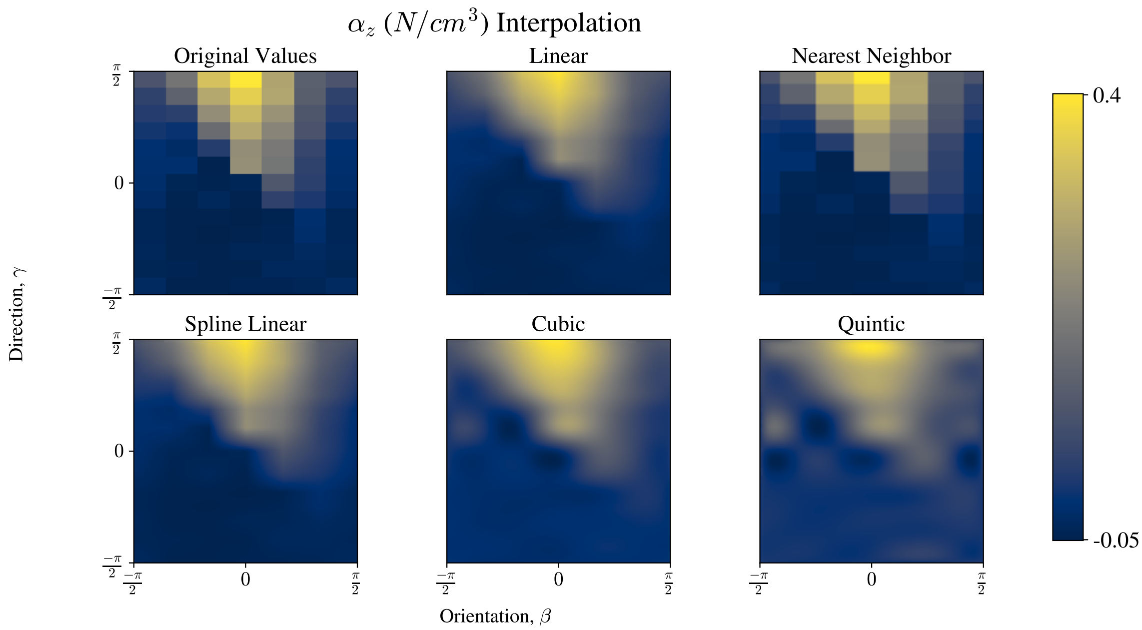

Figure 2.6: Comparison of spatial interpolation methods for vertical stresses per unit depth, a_z. The original values are depicted as a contour plot in the bottom right corner. The original data is interpolated to include values for intermediate grid points. Starting from the top left corner, the methods of interpolation examined include linear, nearest neighbors, spline linear, cubic, and quintic.

Initially, the resistive forces per unit depth data were organized on a regular grid with non-uniform spacing, formed by different β and γ values. To assess the predictive capabilities of different multivariate interpolating methods, several test points were selected. Then, the resistive forces were interpolated on these test points to evaluate the accuracy of the predictions against the true values. As demonstrated in Fig. 2.6 and 2.7, the true values are reproduced by all of the methods to some extent. However, for achieving smooth and continuous distributions of the resistive stresses, both linear and spline interpolations of first order yielded the most favorable and comparable results. Given that the linear method is less computationally expensive, it was selected as the preferred method for producing additional grid data points to estimate forces.

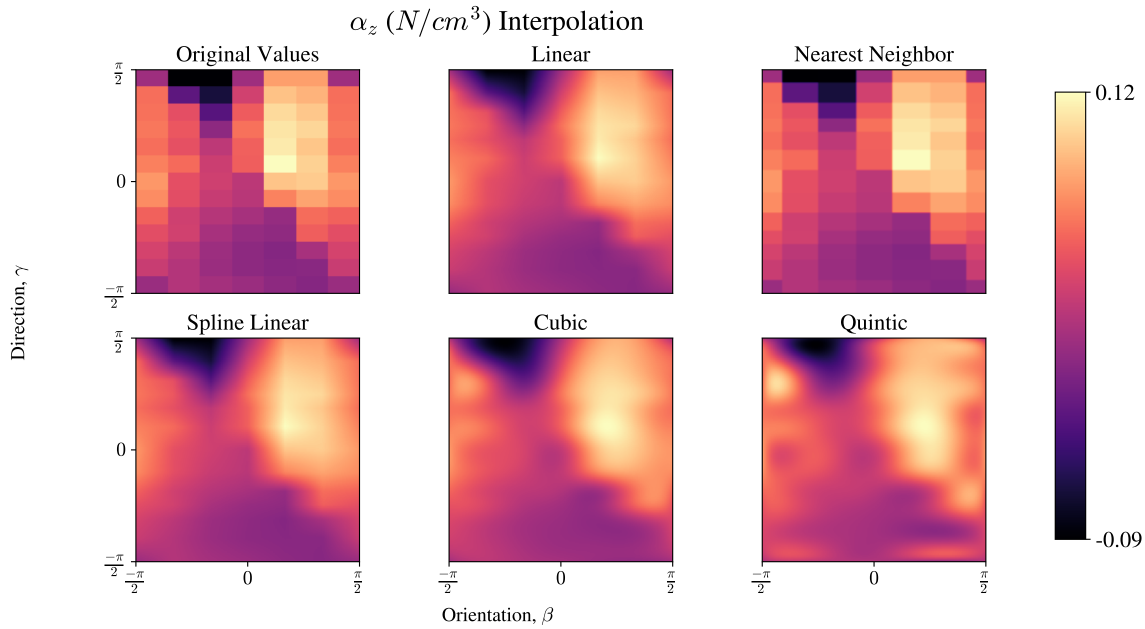

Figure 2.7: Comparison of spatial interpolation methods for horizontal stresses per unit depth, a_x. The original values are depicted as a contour plot in the bottom right corner. The original data is interpolated to include values for intermediate grid points. Starting from the top left corner, the methods of interpolation examined include linear, nearest neighbors, spline linear, cubic, and quintic.

2.2.2 Flat Leg

In the study, the initial configuration examined involves a flat leg, measuring L in length and w in width. This leg is then separated into n equally sized elements. After placing the leg at a hip height of $h = 2\,\mathrm{cm}$ above the ground surface, this leg undergoes rotation within the granular media. Throughout each stage of the rotation, the orientation and depth of each element vary, resulting in a diverse distribution of resistive forces experienced along the length of the leg.

A representation of the flat leg configuration is provided in Fig. 2.8, with an enlarged view of a single leg element on the right side to illustrate the kinematic parameters more clearly. In

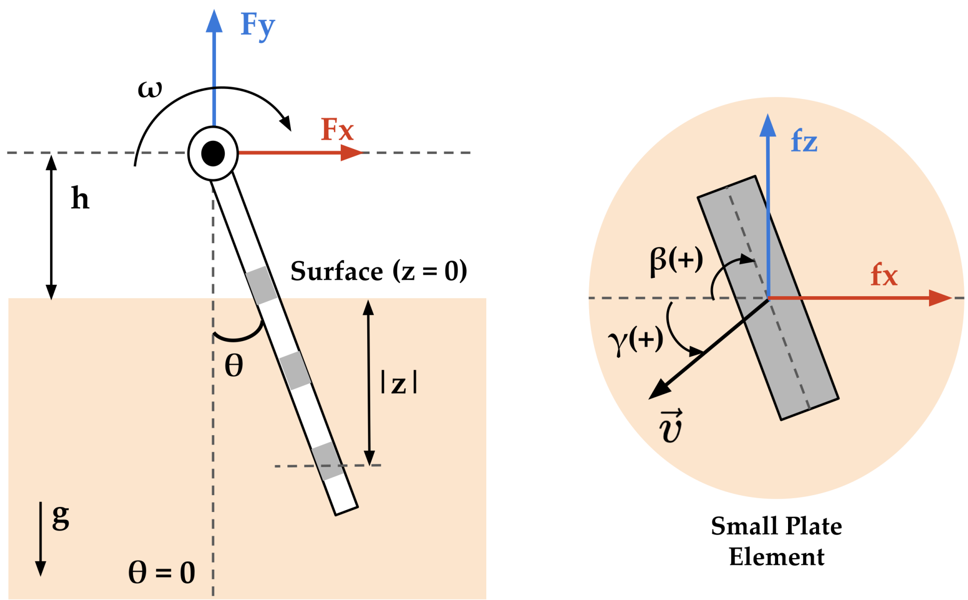

Figure 2.8: Representation of resistive forces for a flat leg element rotating within a granular media bed at a fixed hip height. The orientation of an individual leg element is determined by the angle of attack β and angle of intrusion γ.

this representation, the sign convention for the angle of attack, β, dictates that it is considered to be positive when the front side of the element is positioned above a horizontal line passing through its centroid. Similarly, the intrusion angle, γ, is defined as positive when the velocity vector points in a direction below the horizontal line and negative when the velocity vector points upward. This sign convention facilitates a consistent interpretation of the angular parameters throughout the analysis.

In Fig. 2.9, the sequential rotation of the leg is illustrated, starting from an initial negative angle $\theta = -90°$ and gradually progressing to positive angles until reaching $90°$. During the negative θ phase, the leg is in its intrusion stage, whereas as θ becomes positive, the leg enters the extraction phase. In this study, it is assumed that each leg element moves akin to a pendulum, where the associated velocity vector is always tangent to the arc of the element.

Analysis carried out the kinematics of both the intrusion and extraction phases separately.

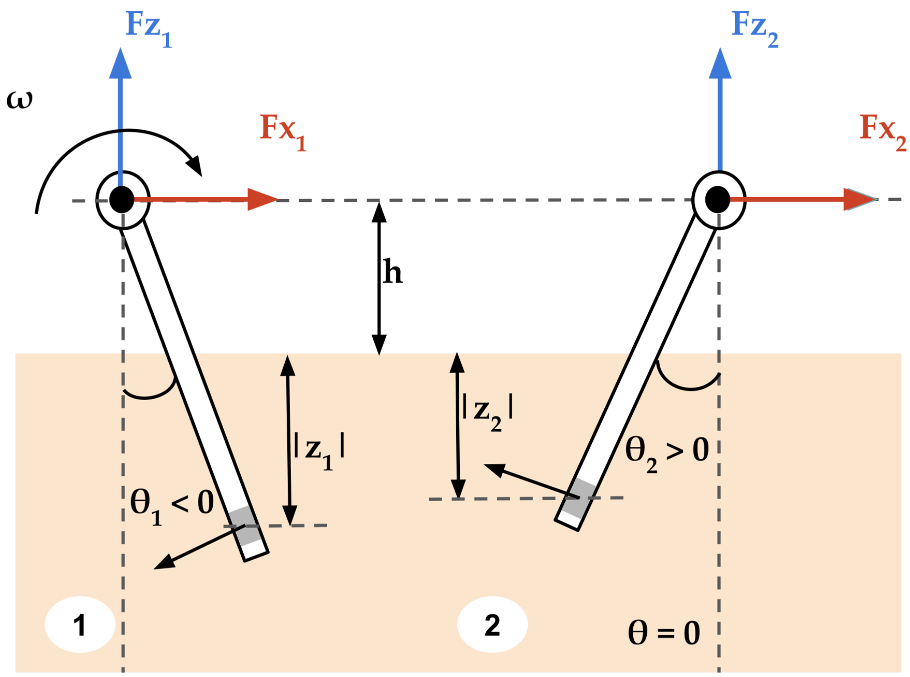

Figure 2.9: Rotating leg layout for the intrusion (1) and the extraction (2) stages of gait.

By isolating a single element and modeling it as a pendulum, one can arrive at the schematic representation shown in Fig. 2.10. In accordance with the established sign convention, the element experiences a positive attack angle ($\beta > 0$) and a positive intrusion angle ($\gamma > 0$) in the intrusion phase illustration shown in Fig. 2.10a. Within this schematic, the centroid of the element is denoted as A, the point on the axis of rotation as O, and the point of intersection between the horizontal and vertical lines as B. These three points form a right triangle $\triangle OAB$. Given the negative value of θ during the penetration phase, the angle β can be derived as follows:

$$\beta = \frac{\pi}{2} - |\theta| \tag{2.8}$$

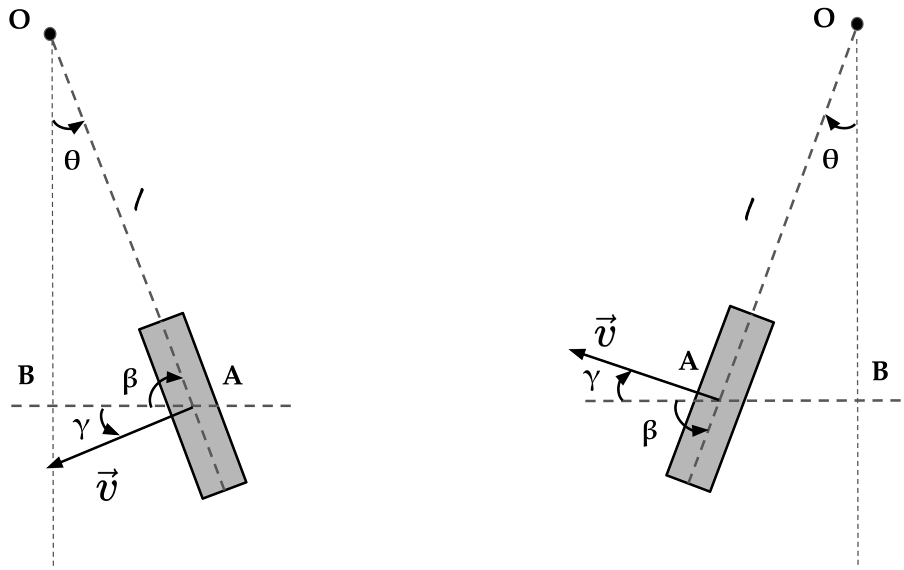

(a) Intrusion

(b) Extraction

Figure 2.10: Kinematic diagram of a leg element during the intrusion (a) and the extraction (b) stage.

As β and γ are complementary angles, the intrusion angle can be determined as:

$$\gamma = \frac{\pi}{2} - \beta \tag{2.9}$$

To determine the resistive forces on a leg element accurately, it's also essential to calculate the element's depth from the surface of the granular media. In the scenario of a flat leg with a length of L split into n elements, and i denoting the increment of the elements from the top of the leg, the radial distance between the centroid of the i^{th} element and point O is given by:

$$l = \frac{L}{n}\left(i - \frac{1}{2}\right) \tag{2.10}$$

Subsequently, the depth of the i^{th} element (z_i) corresponds to the length of segment $\overline{OB}$, as depicted in Figure 2.10a. Trigonometry is employed to calculate this depth:

$$z_i = \overline{OB} = l \sin \beta \tag{2.11}$$

Similarly, the same variables can be derived for the extraction phase. As depicted in Figure 2.10b, $\theta > 0$, while β and γ have the same magnitudes they have opposite signs compared to their counterparts during the intrusion phase.

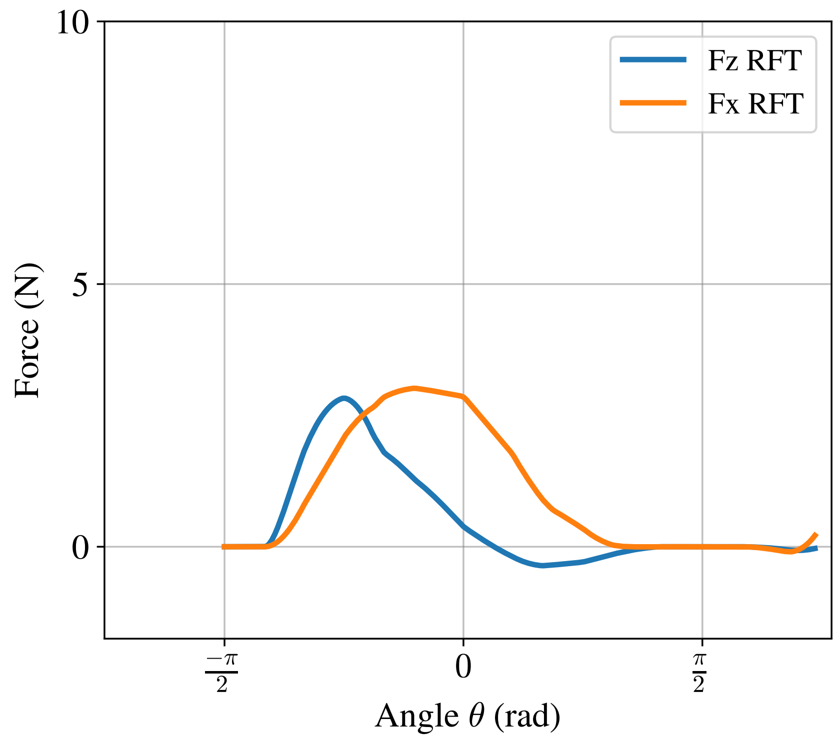

Figure 2.11: Resistive forces diagram for a flat leg of maximal length $L = 7.62\,\mathrm{cm}$ and width $w = 2.54\,\mathrm{cm}$ rotating from a hip height $h = 2.00\,\mathrm{cm}$ with an angular speed $\omega = 0.20\,\mathrm{rad/s}$.

After computing the variables for all examined θ values, the corresponding horizontal and vertical stresses per unit depth (a_x, a_z) can be determined by utilizing the interpolated grid data. Applying Eqs. (2.6) and (2.19) to each incremental element, and after linearly superposing them, the results for resistive forces are obtained. For a maximal length of $L = 7.62\,\mathrm{cm}$ and a width of $w = 2.54\,\mathrm{cm}$, the resistive forces across various θ values form bell-shaped curves, as depicted in Fig. 2.11. Notably, F_z and F_x reach nearly the same maximum magnitude. However, the resistance in the vertical direction peaks towards the beginning of the leg penetrating the media, whereas the horizontal resistance is higher during the leg's transition into the extraction phase.

2.2.3 C-shaped Leg

The equations describing resistive forces for the C-shaped leg case are formulated by analyzing a C-shaped leg characterized by a length of $2R$ and a width of w, where R is the radius of the leg's semicircular geometry. Following a methodology akin to that of the flat leg case, the leg is divided into n equally sized elements and is then placed at a hip height of $2.00cm$ above the granular media. It is worth noting that the θ angle is measured between the vertical line passing through the axis of rotation to the diameter joining the extremities of the leg's arc. To ensure that the leg starts rotating from a position where it is not in contact with the granular media, the initial angle is $\theta_0 = 135°$.

As the C-shaped leg is rotated, the kinematic parameters of each of the n elements are analyzed. The angles of orientation for one of the elements during the intrusion phase ($\theta < 0$) are illustrated in Fig. 2.12. Employing geometry and trigonometry principles, the following relations for $\theta < 0$ are derived:

$$\begin{cases} \phi = \frac{\pi}{2} - (\alpha - |\theta|) \\ \phi + |\beta| = \frac{\pi}{2} \end{cases} \tag{2.12}$$

where angle α for the i^{th} element out of the total n elements across the leg's arc can be expressed as:

$$\alpha = i\frac{\pi}{n} \tag{2.13}$$

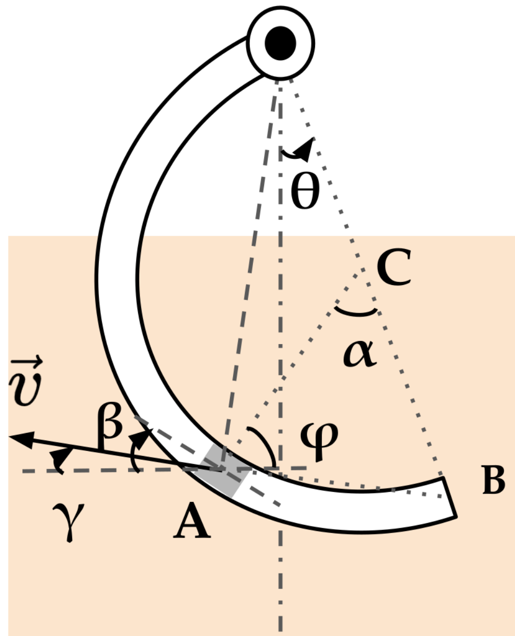

Figure 2.12: Kinematic diagram of an element within a C-shaped leg during the intrusion stage of the gait.

Assuming a pendulum-like motion for each element relative to point O, the velocity is perpendicular to the line connecting the centroid of the element to O. With this assumption influencing the γ variable, the following equations can be derived by analyzing triangle $\triangle OAB$ inscribed in the semicircle, as well as triangles $\triangle CAB$, and $\triangle OAC$ within the schematic shown in Fig. 2.12:

$$\begin{cases} \angle AOB + \angle OBA = \frac{\pi}{2} \\ \phi + |\gamma| = \angle ABC \\ 2\angle ABC + \alpha = \pi \end{cases} \tag{2.14}$$

From Eqs.(2.13) and (2.14), the magnitudes for β and γ can be determined from:

$$\begin{cases} |\beta| = \alpha - |\theta| \\ |\gamma| = \frac{\alpha}{2} - |\theta| \end{cases} \tag{2.15}$$

For elements positioned within the leg such that $\alpha > |\theta|$, the leg's orientation yields $\beta > 0$ and $\gamma < 0$. Conversely, for elements where $\alpha < |\theta|$, the orientation angles result in $\beta < 0$ and $\gamma > 0$. To adhere to the chosen sign convention, the orientation angles are defined as follows for the case when the leg penetrates the granular media:

$$\begin{cases} \beta = \alpha - |\theta| \\ \gamma = -(\frac{\alpha}{2} - |\theta|) \end{cases} \tag{2.16}$$

Following the same methodology to derive the orientation angles during the extraction stage of the gait ($\theta > 0$), the angles of attack and intrusion become:

$$\begin{cases} \beta = \alpha + \theta \\ \gamma = -(\frac{\alpha}{2} + \theta) \end{cases} \tag{2.17}$$

By also incorporating the i^{th} element's depth variable, the resistive forces equations at a certain angle θ are derived as:

$$\begin{cases} F_z = \sum\limits_{i=1}^{n} \sigma_z(\beta_i, \gamma_i, R(\cos\theta + \cos\beta_i))A_i \\ F_x = \sum\limits_{i=1}^{n} \sigma_x(\beta_i, \gamma_i, R(\cos\theta + \cos\beta_i))A_i \end{cases} \tag{2.18}$$

where A_i is each element's bottom area, defined as:

$$A_i = \frac{\pi R w}{n} \tag{2.19}$$

For a C-shaped leg with a length of $2R = 7.62\,\mathrm{cm}$ and width $w = 2.54\,\mathrm{cm}$, after employing the derived kinematic parameters to estimate the corresponding stresses per unit depth and subsequently superposing the results for all the leg elements, the results shown in Fig. 2.13 are generated. When compared to the case of a flat leg with the same dimensions, the C-shaped leg undergoes significantly larger vertical forces while interacting with the granular media. Similar to the flat leg, the C-shaped leg encounters greater resistance in both x and z directions during intrusion than during extraction.

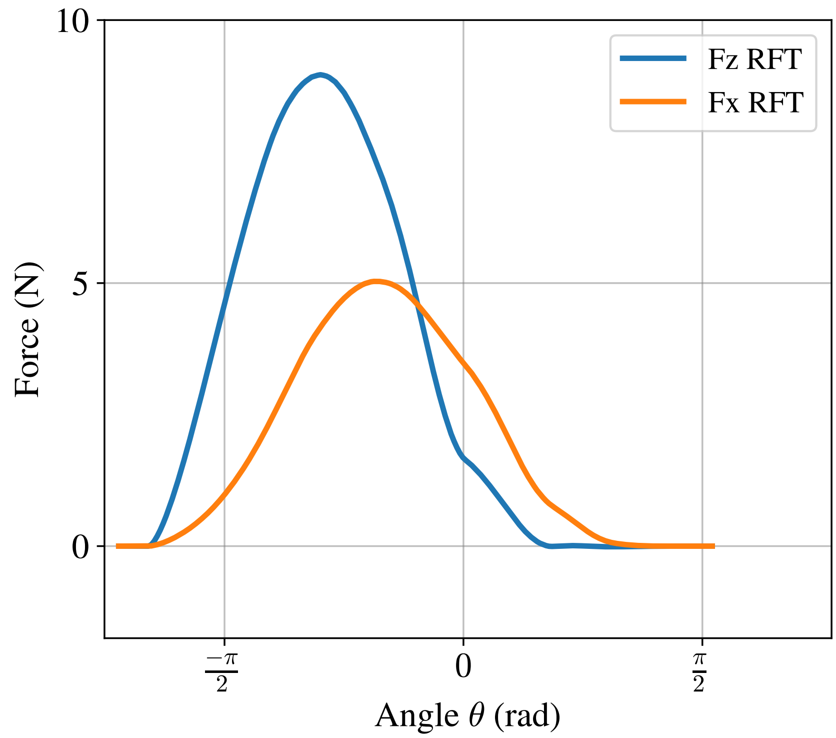

Figure 2.13: Resistive forces diagram for a C-shaped leg of maximal length $L = 7.62\,\mathrm{cm}$ and width $w = 2.54\,\mathrm{cm}$ rotating from a hip height $h = 2.00\,\mathrm{cm}$ with an angular speed $\omega = 0.20\,\mathrm{rad/s}$.

2.2.4 Reverse C-shaped Leg

The analysis is also extended to a reverse C-shaped leg by employing a methodology analogous to that used for the flat leg and C-shaped leg cases. Here, a reverse C-shaped leg, characterized by a maximal length of $2R$ and a width of w is considered. Similar to the previous cases, the reverse C-shaped leg is divided into n equally sized elements and is placed at a hip height of $2.00\,\mathrm{cm}$ above the granular media. The initial angle is set to $\theta_0 = 135°$.

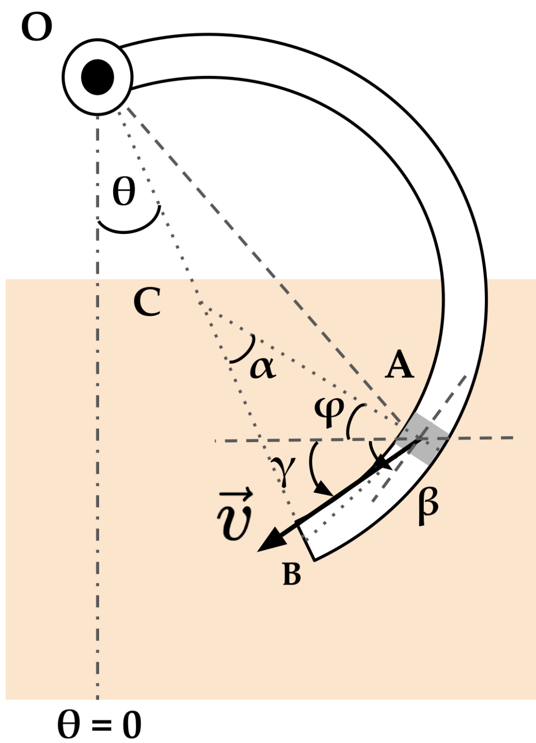

Figure 2.14: Kinematic diagram of an element within a reverse C-shaped leg during the intrusion stage of the gait.

As the reverse C-shaped leg is rotated, the kinematic parameters of each element are once again examined. The angles of orientation of an element during the intrusion phase ($\theta < 0$) are depicted in Fig. 2.14. After utilizing geometric and trigonometric principles, the following relations for intrusion ($\theta < 0$) are derived:

$$\begin{cases} \phi = \frac{\pi}{2} - (\alpha + |\theta|) \\ \phi + |\beta| = \frac{\pi}{2} \end{cases}, \tag{2.20}$$

Here, the angle α for the i^{th} element can be expressed similarly to that for the C-shaped leg:

$$\alpha = i\frac{\pi}{n} \tag{2.21}$$

By considering the velocity perpendicular to the line connecting the centroid of the element to O, the following relations can be derived through the analysis of the relevant triangles:

$$\begin{cases} \angle AOB + \angle OBA = \frac{\pi}{2} \\ \phi + |\gamma| + \angle OAC = \frac{\pi}{2} \\ 2\angle OBA + \alpha = \pi \end{cases} \tag{2.22}$$

From Eqs. (2.24) and (2.22), the magnitudes for β and γ can be expressed as follows:

$$\begin{cases} |\beta| = \alpha + |\theta| \\ |\gamma| = \frac{\alpha}{2} + |\theta| \end{cases} \tag{2.23}$$

For $\alpha + |\theta| < 90°$, the leg's orientation yields $\beta < 0$ and $\gamma > 0$. To maintain consistency with the sign convention, the orientation angles for when the leg intrudes the media are defined as follows:

$$\begin{cases} \beta = -(\alpha + |\theta|) \\ \gamma = \frac{\alpha}{2} + |\theta| \end{cases} \tag{2.24}$$

On the other hand, during extraction ($\theta > 0$), the angles are expressed as:

$$\begin{cases} \beta = -(\alpha - \theta) \\ \gamma = \frac{\alpha}{2} - \theta \end{cases} \tag{2.25}$$

By finally implementing the depth variable for each element i, the resistive forces become:

$$\begin{cases} F_z = \sum_{i=1}^{n} \sigma_z(\beta_i, \gamma_i, R(\cos\theta + \cos\beta_i))A_i \\ F_x = \sum_{i=1}^{n} \sigma_x(\beta_i, \gamma_i, R(\cos\theta + \cos\beta_i))A_i \end{cases} \tag{2.26}$$

By estimating the resistive forces for a range of θ angles for a reverse C-shaped leg with a length of $2R = 7.62\,\mathrm{cm}$ and a width of $w = 2.54\,\mathrm{cm}$, the generated results are illustrated in Fig. 2.15. From a comparison of these results with those obtained in the previous two cases, it is seen that there is a significant reduction in the magnitudes of the lift forces. Particularly noteworthy is the substantial region where there are negative lift forces, indicating the presence of a suction effect during the extraction phase of the leg.

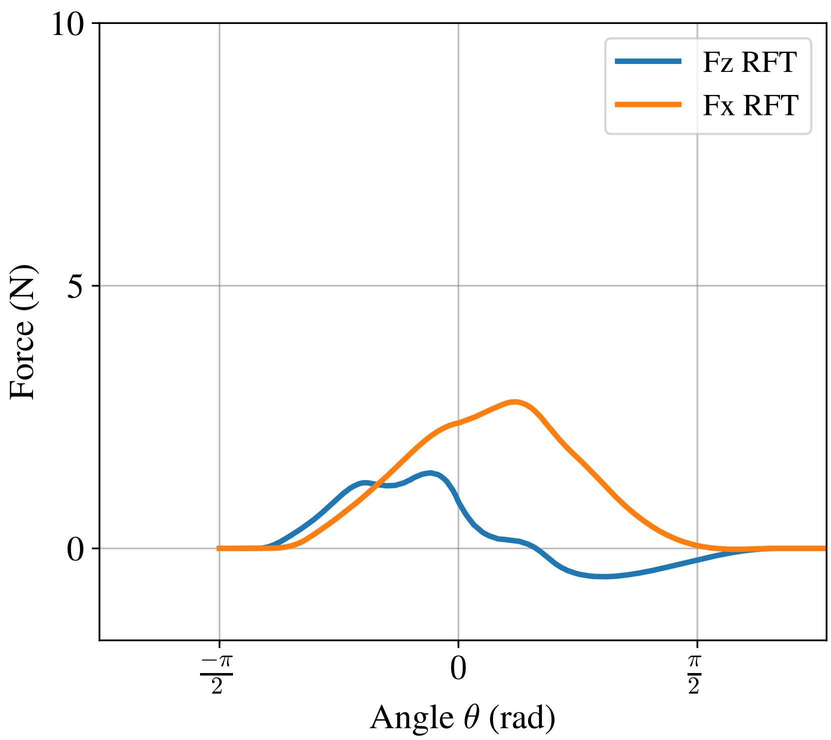

Figure 2.15: Resistive forces diagram for a reverse C-shaped leg of maximal length $L = 7.62\,\mathrm{cm}$ and width $w = 2.54\,\mathrm{cm}$ rotating from a hip height $h = 2.00\,\mathrm{cm}$ with an angular speed $\omega = 0.20\,\mathrm{rad/s}$.

2.3 Comparison with SPH Results and Experimental Data

In the following section, a comprehensive comparison amongst the results obtained from the RFT model, the SPH model, and experimental data [11] is presented. To provide an efficient comparison of the datasets, the input parameters of the legs and granular particles must be consistent to prevent the introduction of biases. In this study, the intruder's leg measures $2R = 7.62\,\mathrm{cm}$ in length, $d = 2.54\,\mathrm{cm}$ in width, and $t = 0.64\,\mathrm{cm}$ in thickness. Respectively, the granular media for both models consists of glass spheres in a closely packed state with a diameter of $d = 3.00\,\mathrm{mm}$. After simulating the leg and granular substrate similarly in both models, the comparison necessitates a leg rotation test within the granular media and the concurrent evaluation of the net vertical and horizontal forces.

When employing the RFT based model for a leg rotation test, the granular intrusion must occur within the quasi-static limit. Since the RFT model is a simplified, reduced-order model, it can only capture locomotive behavior at low speeds where the interactions between the intruder and the ground are rate-insensitive and the granular particles have time to rearrange their positions to achieve a balance between internal and external forces [4]. For this reason, in both model tests, the leg is rotated clockwise at a slow speed of $\omega = 0.2\,\mathrm{rad/s}$ from angle $\theta = -135°$ to $\theta = 135°$.

The variations in the x and z force responses as determined by using the RFT based model and the SPH based model are illustrated in Figure 2.16. The solid lines correspond to RFT model based predictions while the lines with the circular markers correspond to SPH model based predictions. In addition, three different cases of leg geometries are analyzed. In the first column of Fig. 2.16, the results for a C-shaped leg are illustrated, while the responses of a flat leg and a reverse C-shaped are examined in the two other columns of Fig. 2.16. As can be inferred

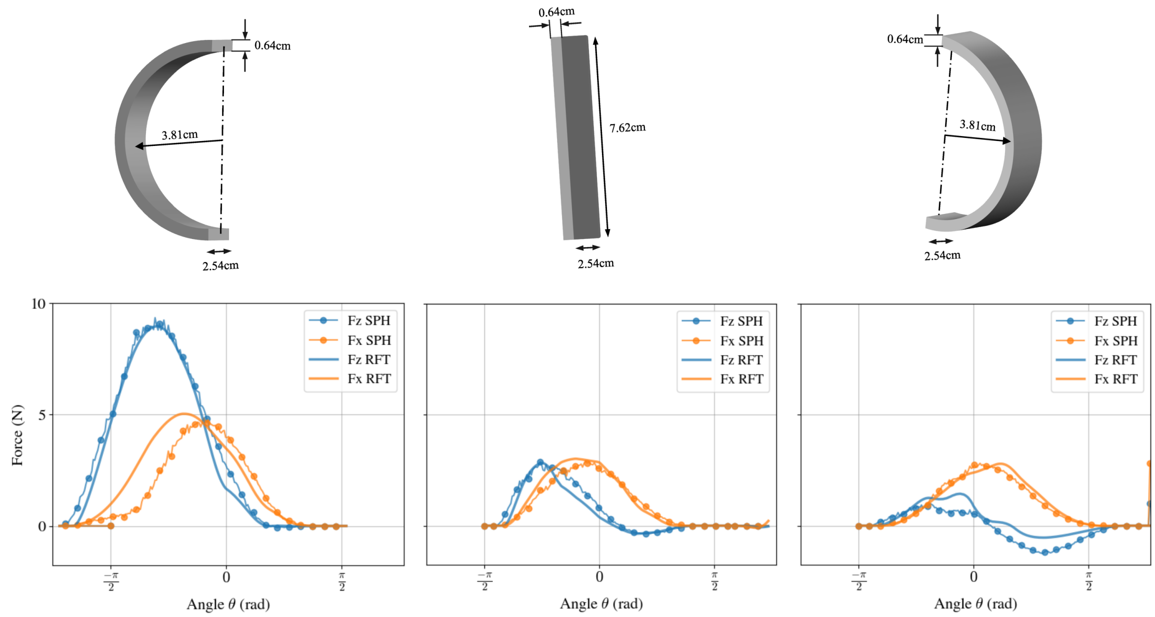

Figure 2.16: Comparison of the net resistive forces determined during a rotation test of a flat leg, a C-shaped leg, and a reverse C-shaped leg as estimated by using the RFT and SPH models. The RFT model based results are shown by using solid lines while the SPH model based results are shown by using lines with markers. Furthermore, the orange-colored curves correspond to the drag resistance forces F_x, and the blue-colored curves correspond to the lift resistance forces F_z, whose peak values tend to be higher.

from these figures, there is comparable agreement between the RFT and SPH results, with similar peak values for net lift and drag. Strikingly, the peak lift values for the C-shaped leg vary by just 0.3% and the peak drag values vary by 5.3%. For the flat leg, there is a 8.9% difference in lift and a 15.2% difference in drag.

In the cases of the flat and reverse C-shaped legs, it is also worth mentioning that the suction lift effect is visible in both models. During the extraction phase of these two leg morphologies, the lift forces take on negative values, indicating that the legs are being dragged downwards, and thus, for these two leg geometries, it would be more difficult to withdraw from the granular media [22]. The displacements of the granular particles around the intruding legs cause this effect, also known as negative buoyancy. Notably, a flat leg and a reverse C-shaped leg rotating through a granular material can form a cavity directly beneath themselves during extraction. Granular particles tend to preserve shape or configuration stability and reduce pressure differences, and hence, it can be expected that they will try to migrate to fill the void [2]. This effort to collapse into the cavity rather than support the legs from below can result in a net downward force on the legs, known as suction. As seen in Fig. 2.16, the empirical RFT model based predictions and SPH's particle interaction modeling based predictions both consistently capture this phenomenon for the flat and the reverse C-shaped leg cases.

Interestingly, it can also be observed in Fig. 2.16, that both models show an analogous asymmetry in the net resistive forces with respect to the vertical direction of the legs, when $\theta = 0$. Clearly, the blue bell-shaped curves, which represent the net lift forces for a full leg rotation, appear to peak during the intrusion phase ($\theta \leq 0$). This demonstrates that the leg, regardless of shape, encounters greater vertical resistance when it penetrates the granular media than when it exits it. This asymmetry in lift resistance between the intrusion and withdrawal phases is caused by the existence of increased friction, jamming, and arching, which ultimately impede the leg's invasive movement. By contrast, the asymmetry in drag forces, as indicated by the orange-colored curves for both RFT and SPH model based predictions, is not as pronounced as it is for the determined lift forces, as the granular particle's freedom of movement in the horizontal direction is bounded [10].

The comparison between results obtained from the RFT model and those from a higher-fidelity model revealed a considerable consistency in the force predictions under similar conditions. However, to gain further insights into the validity of the reduced-order model's outcomes, it was imperative to also compare them with experimental findings. In a study conducted by Li *et al.* [11], experiments where carried out where net resistive forces experienced

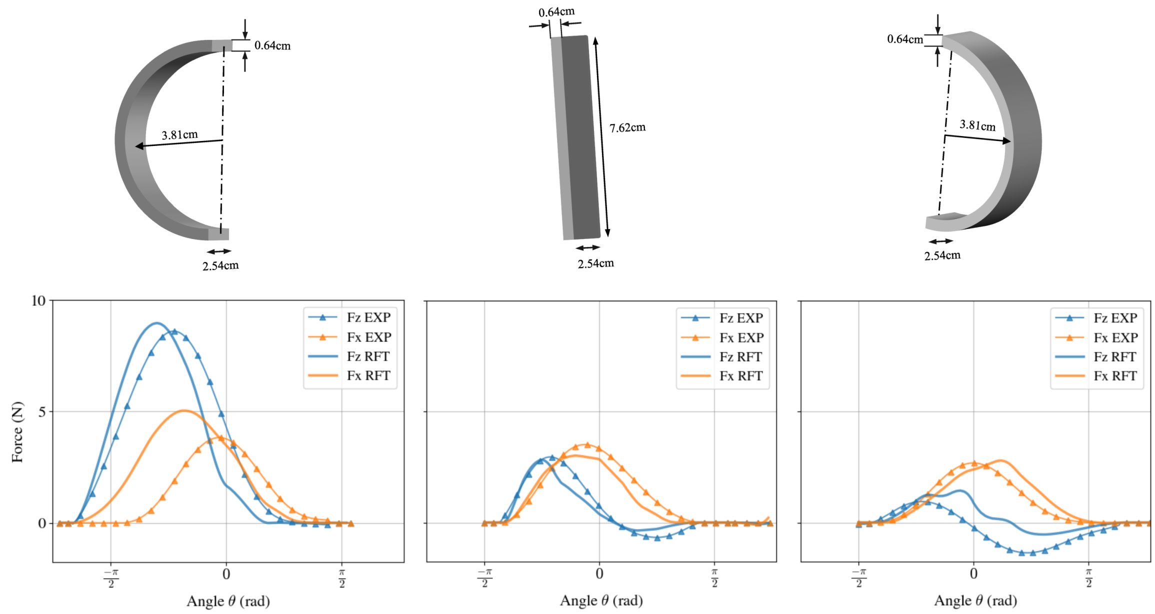

Figure 2.17: Comparison of the net resistive forces determined during a rotation test of a flat leg, a C-shaped leg, and a reverse C-shaped leg as estimated by using the RFT model and experimental data obtained by Li *et al.* [11]. The RFT model based results are shown by using solid lines while the experimental results are shown by using lines with markers. Furthermore, the orange-colored curves correspond to the drag resistance forces F_x, and the blue-colored curves correspond to the lift resistance forces F_z, whose peak values tend to be higher.

by different leg morphologies moving over a container of poppy seeds were directly measured. The results from both the RFT model and the experiments are depicted in Fig. 2.17, with solid lines representing the RFT model's predictions and the lines with markers representing experimental observations.

Even though there is considerable similarity between the RFT model based results and the corresponding experimental data in most cases, discrepancies arise in the case of a C-shaped leg for the horizontal forces F_x, particularly, in the θ angle at which the peak force occurs. This discrepancy is further illustrated in Fig. 2.18a, where the mean square errors (MSEs) for the C-shaped leg's F_x between the RFT model's and the experimentally obtained estimations are notably higher than the MSE errors observed in the other cases. The differences could stem from the oversimplified assumption in the RFT model regarding the pendulum-like direction of each individual leg element, which impacts the amount of calculated stress the leg experiences. While this assumption may align well with the directions of the elements in the flat leg case, it might not accurately represent reality in the context of a C-shaped leg case. When the C-shaped leg case is excluded, the MSE errors between the results of the reduced-order model and the experimental observations are found to be significantly low for the remaining two leg geometries. This suggests that despite being empirical and simplified in nature, the RFT model could be valuable for certain leg geometries. One needs to use this model with caution for getting force estimates under specific circumstances, such as during slow movements over granular media.

Based on the above findings, it appears that one can use both RFT and SPH based models to capture the locomotive responses of three leg morphologies rotating in granular media at a low speed, since they yield comparable peak values for lift F_z and drag F_x forces. Of course, as the RFT based model is a simplified model, it can only be used to reasonably simulate locomotion under rate-insensitive conditions. By employing an empirical extension of the considered model, it becomes possible to use RFT based models for further scenarios of locomotion in granular media. However, since the empirical version relies on experimental data, the use of RFT based models can be limited to less intricate cases. On the contrary, the SPH model does not require the collection of experimental data. Additionally, one can study the rate effect in granular intrusion by being able to simulate leg interactions for higher speed regimes. The downside of using an SPH based model is the fact that it is substantially more computationally expensive than a RFT based model, which makes the latter quite appealing for simple terramechanics problems.

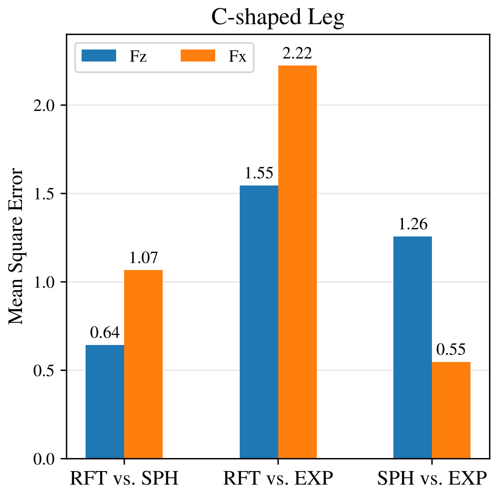

(a)

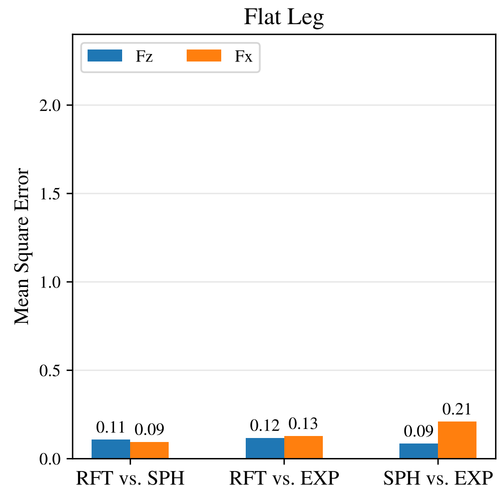

(b)

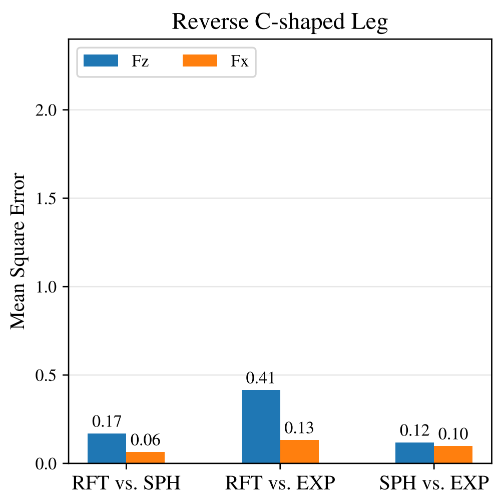

(c)

Figure 2.18: Mean Square Errors (MSEs) for comparisons amongst force predictions generated by the RFT model, the SPH model, and experimental observations. Each set of bar plots within the figure illustrates the MSE errors for three specific comparisons, namely between the RFT and SPH models, the RFT model and experimental data, and the SPH model and experimental data. In subplot 2.18a, the focus is on a C-shaped leg analysis, while in subplots 2.18b and 2.18c, the focus is on a flat leg and a reverse C-shaped leg, respectively. The orange-colored bars represent the MSE errors in the horizontal forces F_x and the blue-colored bars correspond to the vertical forces F_z.

2.4 RFT Model Based Studies for Human-Sized Robotic Appendage

Having validated the RFT based model by comparing the force estimations from this model to the results obtained by using the high-fidelity model based on SPH, the RFT based model is subsequently used to estimate the forces for a human-sized leg morphology interacting with granular media. In particular, the human-like leg design is simulated as a flat leg like the one studied in Chapter 2.2.2. Here, the hip height is zeroed ($h = 0$), and the maximum angle of rotations is approximately $3°$. Additionally, the geometric parameters are set to a width of $8.5cm$ and a maximal length that could range anywhere between $25.00\,\mathrm{cm}$ to $33.00\,\mathrm{cm}$. Applying the same methodology as described in Chapter 2.2.2, the net forces can be found by splitting the leg into numerous elements, determining the forces on each element, and superposing them.

The results obtained for the estimated net forces are shown in Fig. 2.19. The net forces are depicted in both the horizontal and vertical directions across a range of maximal lengths. It becomes apparent that as the maximal length is increased, the magnitudes of the overall net forces increase too. Furthermore, the estimated drag forces exhibit considerably smaller magnitudes compared to those of the normal forces. This is an indication that during a gait over granular media, the resistance experienced is primarily manifested in the normal direction.

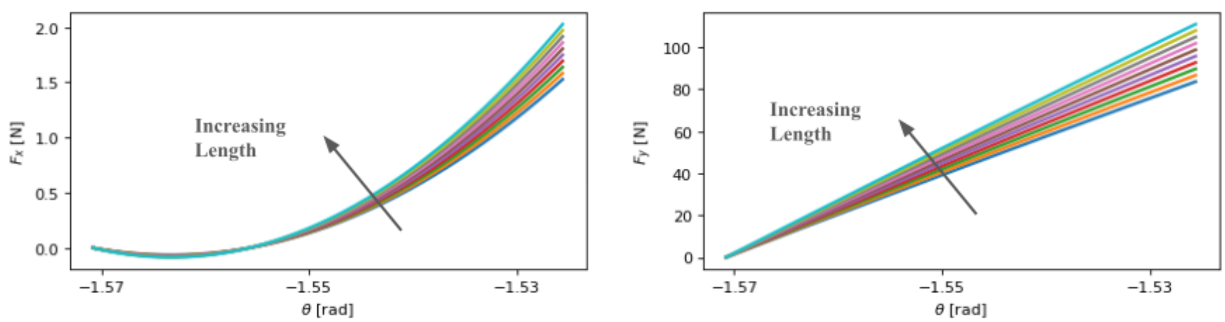

Figure 2.19: Net resistive forces in the vertical and horizontal directions for various leg length designs.

Chapter 3: Experimental Studies of Quasi-Static Movements on Granular Surfaces Using a Robotic Dummy Foot

In this chapter, an experiment conducted is detailed. This experiment was designed to investigate the torque and force characteristics associated with a robotic dummy foot as it traversed a granular surface. The results are used to understand the discrepancies between experimental data and simulation based data regarding normal forces during the interaction between the dummy foot and a granular surface. In the following sections, the author has investigated potential geometric factors contributing to horizontal and vertical resistance and discussed how the experimental data was conditioned.

3.1 Methods and Materials

The experimental setup consists of a dummy foot, which measures approximately $24.80\,\mathrm{cm}$ in length, $8.60\,\mathrm{cm}$ in width, and $3.75\,\mathrm{cm}$ in thickness, and is connected to a robotic device equipped with driver assemblies, motors, and a linear encoder for measuring the instantaneous speeds at different time steps. The dummy foot is driven to rotate within the granular media at a slow pace, simulating quasi-static movement, similar to the conditions outlined in the RFT model. The granular material consists of approximately $2\,\mathrm{kg}$ of poppy seeds contained within a $40.00\,\mathrm{cm} \times 25.00\,\mathrm{cm}$ box. The choice of granular media has been made to replicate real-

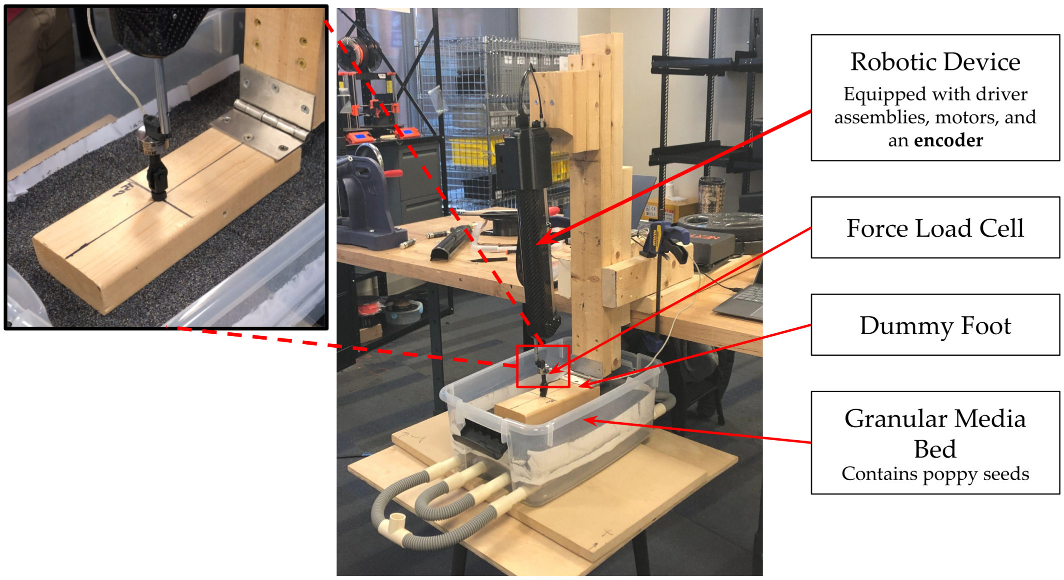

Figure 3.1: Experimental setup for measuring resistance exerted on a rotating dummy foot by the granular media within the container. The setup is comprised of a robotic device connected to a dummy foot that is rotated over a container filled with poppy seeds. In the position where the dummy foot and the robotic device are connected, a load cell is placed to obtain measurements of normal forces. This setup was used to conduct experiments in the facilities of NextStep Robotics in Baltimore, MD.

world scenarios where robotic systems may encounter irregular and deformable terrains. The use of poppy seeds provides a controlled and repeatable experimental environment, and a similar granular medium has been used previously by Li *et al.* [11] in their RFT studies.

As the dummy foot is moved through the poppy seeds, the experimental data are collected in the form of time series data for various parameters, such as the trajectory angle, speed, torque, and force experienced by the leg. Notably, a force load cell is positioned approximately $15.00\,\mathrm{cm}$ away from the foot's axis of rotation. This placement closely aligns with the location where the net normal resistive force is exerted according to the RFT model, which is approximately $16.00\,\mathrm{cm}$ from the axis of rotation.

3.2 Data Collection and Observations

Once the experimental setup was ready, calibration was initiated to test how the dummy foot rotates without disturbing the granular media in the container. Following calibration, an intrusion experiment was conducted three times, maintaining loose compaction of poppy seeds while varying the desired maximum angle of rotation for the dummy foot. In the first trial, with a set trough trajectory angle of three degrees, the actual rotation was only $0.84°$, insufficient for validating the RFT model. In subsequent trials, there were adjustments made to the set trough trajectory angle. For the second trial, this angle was set to $7°$, resulting in a $1.7°$ rotation, while for the third trial, the target was for a $12°$ rotation, achieving approximately $2.6°$ before a connection failure occurred between the dummy foot and the robotic device.

The results of the third trial are shown in Fig. 3.2. In the plot, the recorded commanded angle and speed trajectories are presented alongside their corresponding realized values, offering a comprehensive view of the experimental outcomes. In particular, the blue-colored scattered points correspond to the commanded angle of rotation and actual angle, respectively, while the red-colored scattered points correspond to the commanded angular speed and actual speed, respectively. Notably, despite the intended final angle of rotation of $12°$, the dummy foot was able to achieve only approximately $2.6°$ of rotation. Moreover, the measured torque and force values are displayed in Fig. 3.3, offering insights into the forces exerted during the experiment. Given the small magnitude of the angle of rotation, the measured force from the load cell is considered to be acting normal to the surface of the dummy foot.

In order to validate the resistive forces estimated by the RFT model, a comparison between the experimental normal forces and the ones derived by using the model is shown in Fig. 3.4. A

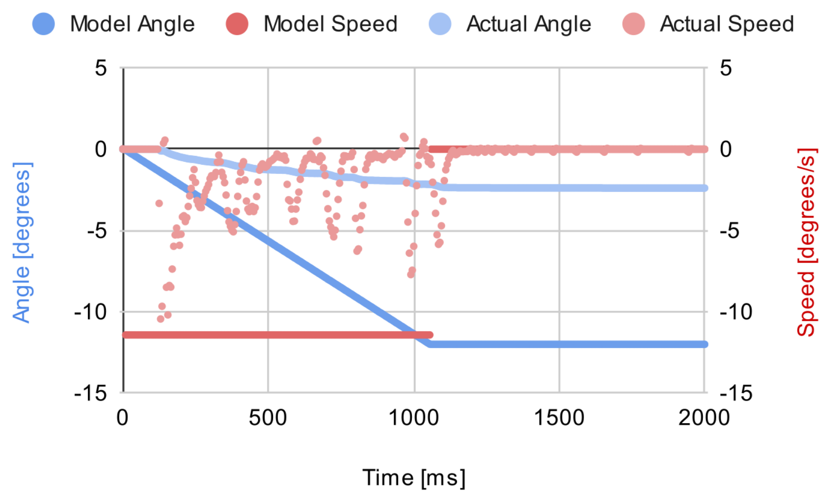

Figure 3.2: Kinematic parameters recorded during the experiment. The x-axis of the plot represents the time (in ms) at which a certain data point was collected. The left y-axis represents angles (in degrees) while the right vertical axis represents angular speed (in degrees/s). The blue-colored scattered points correspond to the desired angle of rotation and actual angle, respectively, and they are associated with the left vertical axis. The red-colored scattered points correspond to the desired angular speed and actual speed, respectively, and they are associated with the right vertical axis.

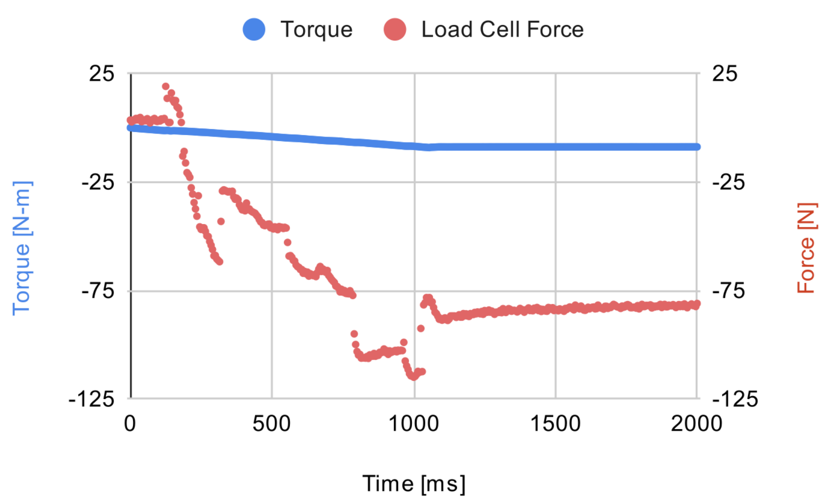

Figure 3.3: Kinetic parameters recorded during the experiment. The x-axis of the plot represents the time (in ms) at which a certain data point was collected. The left y-axis represents torque (in N-m) while the right vertical axis represents forces (in N). The blue scattered points correspond to the input torque and are associated with the left vertical axis. The red scattered points correspond to the normal forces measured from the load cell and are associated with the right vertical axis.

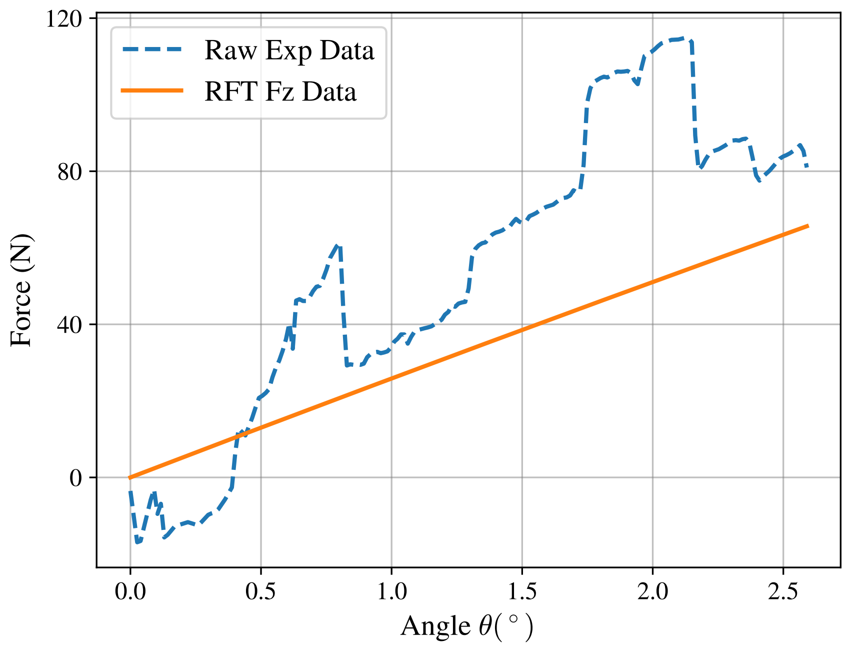

Figure 3.4: Comparison between experimental and model based normal forces.

subtle deviation in the slope between the experimental data and the RFT data remains noticeable. To address this variance, a study is conducted to explore the impact of implementing a higher nominal length in the model's foot as a correction. For this purpose, model parameters are adjusted to refine the match between the experimental data and the RFT model predictions. Additionally, a Butterworth filter is employed to reduce noise in the experimental data. This approach helped enhance the clarity of the comparison between the experimental data and RFT model based data, offering a better understanding of the normal forces at play.

To apply the Butterworth filter, content at a frequency higher than the cutoff frequency is removed. For the given experimental data, the sampling rate is chosen to be $f_s = 200.00\,\mathrm{Hz}$ and the Nyquist frequency is $f_n = 100.00\,\mathrm{Hz}$. The signal content that is above f_n is removed. This low-pass filtering helped smooth out the noisiness of the load cell data in the time-domain. From the filtered data presented in Fig. 3.5, one can see that during the initial phase of data collection,

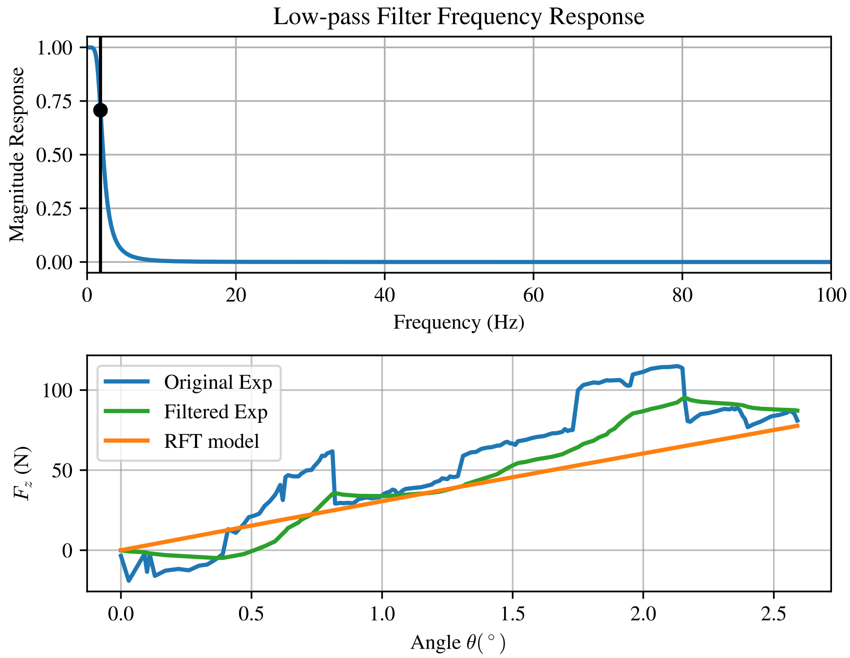

Figure 3.5: Application of Butterworth filter to remove high-frequency content from the experimental data.

certain force values appear to have negative values. Possible contributors to this discrepancy include calibration issues within the experiment or human factors, such as variations in foot positioning that may not align precisely with a flat granular surface at zero hip height. In addition, the filtered data, which are shown by using the green line, are compared with the RFT data, which are shown by using the orange line. After examining different leg lengths within the RFT model, the choice of a maximal length of $27.00\,\mathrm{cm}$ was found to yield a better alignment between the experimental data and theoretical data. This length is $2.00\,\mathrm{cm}$ longer than the dummy foot's actual length during the experiment.

After conducting the experiment and analyzing the results, some observations or concerns noted are as follows:

- Influence of boundary conditions: Concerns remain regarding the potential influence of boundary conditions on the validity of the results. Specifically, the proximity between the foot and the bottom granular surface is considered as a potential source of inaccuracies in the experimental outcomes.

- Comparable consistency between the theoretical and experimental normal forces: For the normal forces, a reasonable alignment is noted between experimental data and model predictions. However, it is observed that the experimental values are more consistent with the model predictions for a larger nominal length of the foot in the RFT model. This suggests a potential adjustment to the RFT model that is needed to enhance accuracy.

Chapter 4: Dynamic Data-Driven Application Systems

In this chapter, the data-driven approach used is detailed. First, an overview of the chosen approach based on Dynamic Data-Driven Application Systems is provided before the studies conducted with the robot appendages and human foot are discussed.

4.1 Overview

To ensure the efficient operation of lower extremity robotic devices over compliant media, a fast and accurate predictor of the leg's dynamical responses is required. The long-term goal is to contribute to the development of a machine learning model capable of detecting and tracking gait events during walking over compliant terrain. For this purpose, the Dynamic Data-Driven Applications Systems (DDDAS) paradigm is used. With this paradigm, one can integrate data from offline physics-based simulations with online sensor measurement data to build a reasonably accurate and cost efficient estimator [23]. For the offline portion of the framework, the simulation datasets are mapped from a high-dimensional to a lower dimensional space through Singular Value Decomposition (SVD). This way, overfitting problems are prevented and model size is decreased, resulting in a drop in the amount of time and storage space needed for the computations. Following the creation of lower-dimensional system data, Gaussian Process (GP) models are trained to produce preliminary estimates of the gait trajectories. However, these

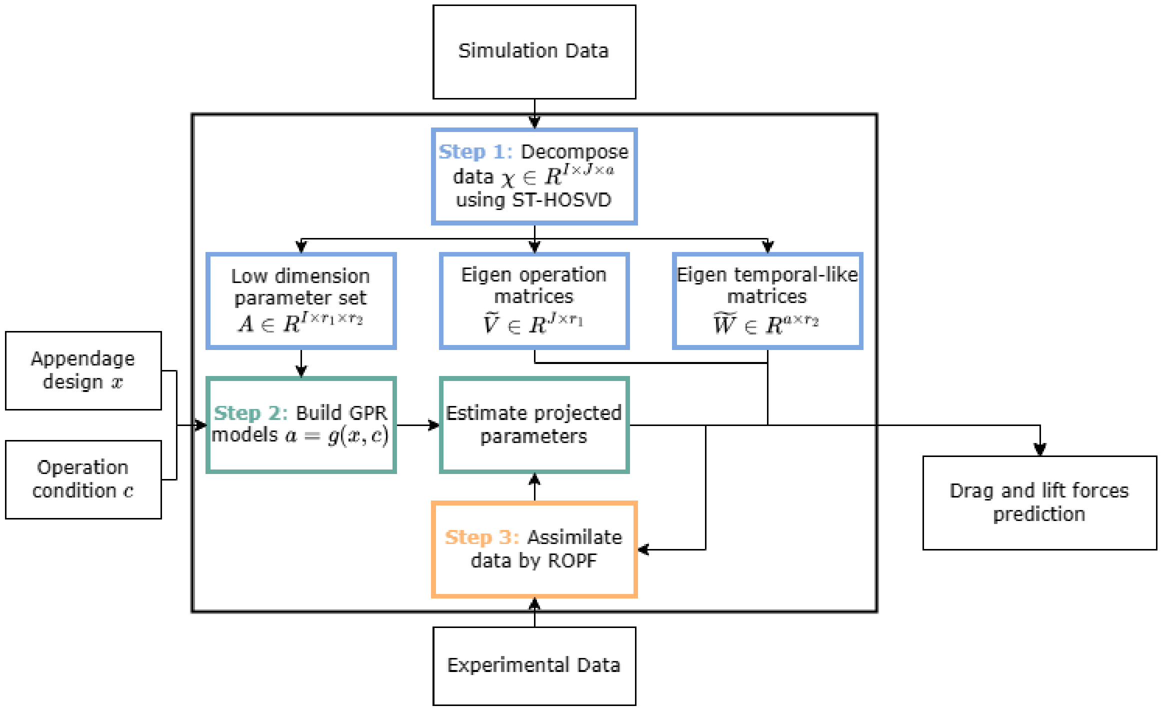

Figure 4.1: Schematic used to illustrate the proposed architecture of the DDDAS framework combining offline simulation datasets with online, noisy sensor observations.

estimates do not represent the approach's final predictions. Instead, a Particle Filter (PF) is used to dynamically update the outputs based on the real-time sensor observations. The remaining portion of this chapter is divided into three sections and used to explain the technical approach used to pre-process the simulation data, perform GP analysis to get preliminary estimations, and employ a PF to update these estimations.

4.1.1 Higher Order SVD

Before the simulation datasets are used to train the DDDAS offline portion, they are first stored in a 3^{rd} order tensor, $\mathcal{A} \in \mathbb{R}^{p_1\times p_2\times p_3}$, with p_1 being the number of layers corresponding to the various angular speeds examined, p_2 being the number of rows corresponding to the time steps within the simulations, and p_3 being the number of columns corresponding to the lift and drag net forces, respectively. Thus, $\mathcal{A}$ is effectively a 3D matrix composed of 2D matrices of size $p_2 \times p_3$ arranged in an array of size p_1.

As the simulation dataset is high-dimensional, the first step is to reduce the dimension of the model and computational cost, by using higher order SVD. The 3D array is unfolded into three separate 2D arrays, $\mathcal{A}_k, k = 1, 2, 3$, each one containing every vector of $\mathcal{A}$ along the first, second, and third dimension, respectively. This technique is commonly referred to as mode-k flattening. In this research, the first dimension corresponds to the model's operating conditions, such as angular speed, the second dimension to time, and the third dimension to forces. Then, the truncated SVD is computed for each 2D matrix separately, so that:

$$\mathcal{A}_k = \boldsymbol{U}_k \boldsymbol{\Sigma}_k \boldsymbol{V}_k^T \tag{4.1}$$

The SVD of each mode-k unfolding of $\mathcal{A}$ generates singular values that can aid in the comprehension of the complex simulation data. Every singular value is associated with a different measurement of importance in terms of retrieving crucial information about the initial data. Plotting the cumulative sum of the explained variance for each dimension, the obtained result is what is shown in Fig. 4.2. This plot can assist in determining how many parameters are required to preserve the necessary information in the original data after dimensionality reduction.

After storing each SVD's left singular vectors, $\boldsymbol{U}_k$, the initial tensor $\mathcal{A} \in \mathbb{R}^{p_1 \times p_2 \times p_3}$ admits a higher order SVD, which can be generalized as:

$$\mathcal{A} \approx \mathcal{S} \times_1 \boldsymbol{U}_1 \times_2 \boldsymbol{U}_2 \times_3 \boldsymbol{U}_3 \tag{4.2}$$

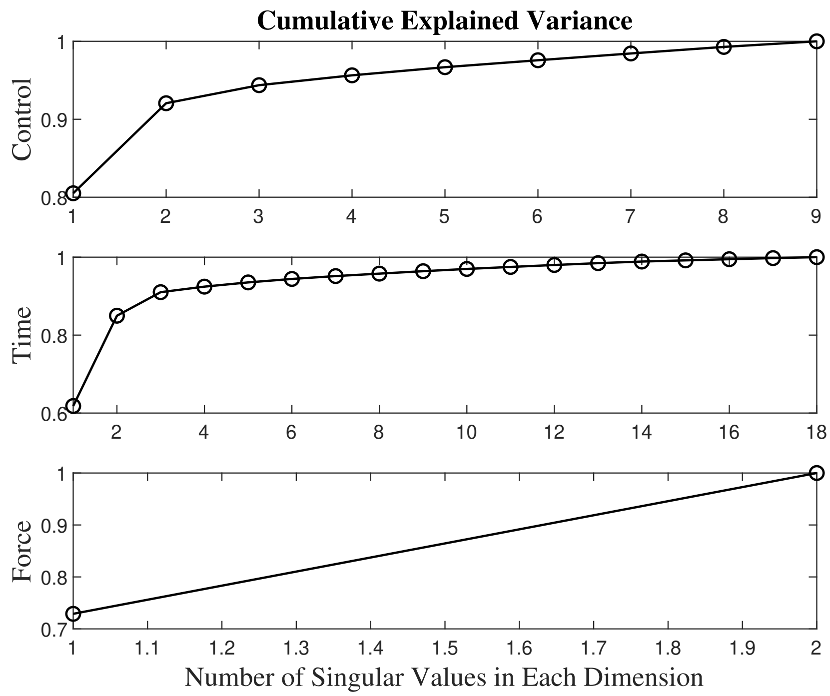

Figure 4.2: Cumulative explained variance in each dimension.

where $\mathcal{S}$ denotes the core tensor and $\boldsymbol{U}_k, k = 1, 2, 3$ denotes the unitary matrices obtained by applying SVD to all mode-k unfolded arrays. Notably, as shown in Eq. 4.3, $\mathcal{S}$ represents the projection of $\mathcal{A}$ onto the tensor basis formed by the singular vectors $\boldsymbol{U}_k$, whereas $\times_k$ symbolizes the k-mode product between a tensor and a matrix.

$$\mathcal{S} = \mathcal{A} \times_{k=1}^{3} \boldsymbol{U}_k^T \tag{4.3}$$

Ultimately, any extraneous rows of $\mathcal{S}$ can be eliminated after identifying the important singular values whose cumulative explained variance is greater than 95%, as indicated in Fig. 4.2. Subsequently, by taking the mode-k product between the core tensor and the set of unitary vectors, an approximation of tensor $\mathcal{A}$ can be calculated using Eq. (4.2).

Furthermore, by computing the mode-k product of the truncated core tensor and the two unitary vectors corresponding to the operational and temporal-like dimensions, $\boldsymbol{U}_k, k = 1, 2$, a new tensor basis is formed. This tensor basis is useful for trajectory predictions. In particular, each estimate of the lift and drag forces with respect to a given angle can be approximated by the mode-k tensor product between the computed tensor basis and a row vector $\alpha = [\alpha_1, \alpha_2, ..., \alpha_D] \in \mathbb{R}^D$ containing the appropriate coefficients, where D is the number of rows of the reduced tensor basis.

4.1.2 Gaussian Process Regression

When higher order SVD is applied to the training simulation dataset, one constructs a tensor basis that represents the most prominent properties of $\mathcal{A}$. As a result, it is assumed in the approach that every gait trajectory may be approximated as the mode-k tensor product between the basis and a row of the corresponding low dimensional coefficients, $\alpha = [\alpha_1, \alpha_2, ..., \alpha_D] \in \mathbb{R}^D$. These low-dimensional coefficients are estimated through GP regression. Specifically, for the GP regression, the training is done by using the row vectors of the coefficients produced by projecting each training dataset within $\mathcal{A}$ onto the tensor basis.

Gaussian Processes, in general, are non-parametric probabilistic models that consist of a set of stochastic variables, $z(\boldsymbol{x}) = [z_1(\boldsymbol{x}), z_2(\boldsymbol{x}), ..., z_D(\boldsymbol{x})] \in \mathbb{R}^D$, where $\boldsymbol{x}$ is the input vector to describe the operational conditions for the predictions. These variables are intended to statistically model the low-dimensional coefficients and they are assumed to follow a multivariate Gaussian distribution. The radial basis function (RBF) kernel multiplied by a constant kernel is used to specify the covariance function for each random variable. The GP models along with the SVD tensor basis are used to predict gait trajectories at a specific angle. Thus, they are stored

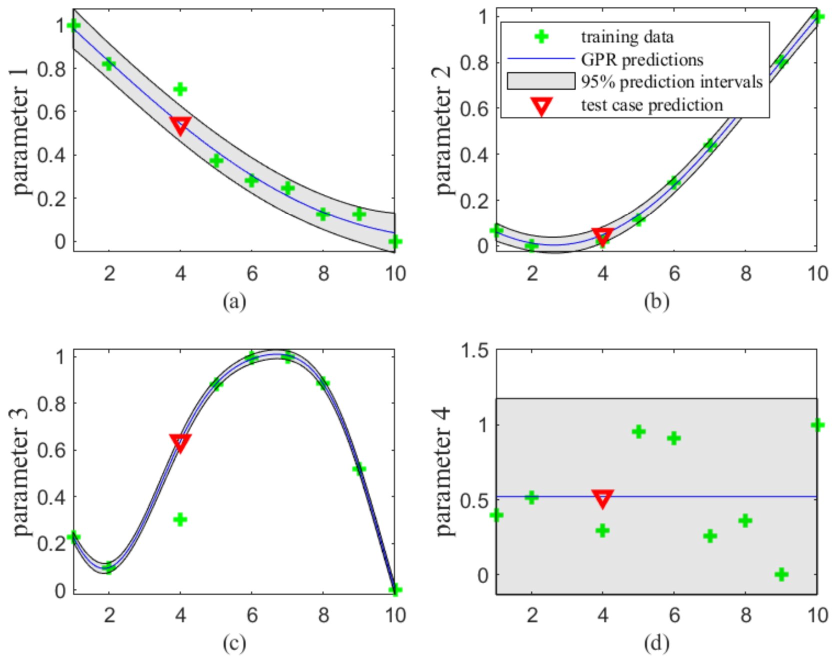

Figure 4.3: GP model predictions of the low-dimensional projected parameters for each operational condition.

offline and will subsequently be accessed online to update the predictions by using a particle filter (PF).

4.1.3 Particle Filter

To further enhance the model's prediction accuracy, sensor measurements can be assimilated in the model through the use of a particle filter. Specifically, the estimations produced by the GP regression and the SVD tensor basis are used as prior distributions for the PF, which then is used to compute the posterior distributions of the stochastic state variables. The PF's ultimate purpose is to update the probability density function (PDF) of all the low-dimensional coefficients $z(\boldsymbol{x}) = [z_1(\boldsymbol{x}), z_2(\boldsymbol{x}), ..., z_D(\boldsymbol{x})] \in \mathbb{R}^D$, according to the dynamical sensor measurements, s_i. Here, the prior PDF of the coefficients is represented by $N = 5000$

sample particles, each with an equal likelihood weight of $w_i = \frac{1}{N}$.

When a sensor measurement is taken at time step i, the posterior weights of each particle are updated. A sensor measurement is denoted as $s_i = o_i + e_i$, where o_i is the observed system response at that specific time step and e_i is the error. It is possible to estimate the likelihood of a sensor measurement by assuming that the error $e_i = s_i - o_i$ follows a normal distribution with a mean at zero. Therefore, the posterior weights can be obtained as:

$$w_i^n = \frac{w_{i-1}^n \cdot p(s_i - o_i)}{\sum_{n=1}^{N} w_{i-1}^n \cdot p(s_i - o_i)} \tag{4.4}$$

where w_{i-1}^n is the prior weight of the nth particle from the previous time step $i-1$. Then, based on the updated posterior weights, multinomial resampling of the state particles is applied. Finally, the coefficient variables are updated and, overall, the PF is used to further enhance the model predictions online.

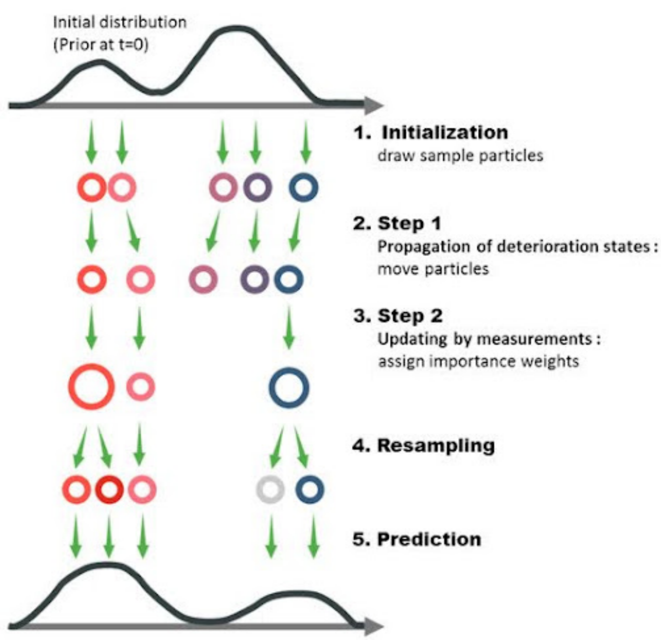

Figure 4.4: Particle filter sequence of steps [24].

4.2 DDDAS Case Study for Robotic Appendage

In this section, an effort is made to evaluate the capacity of DDDAS to accurately predict the nonlinear interaction between a leg and granular media for the different leg configurations presented earlier in this thesis. First, a case study of a small flat leg, as examined in Chapter 2.2.2, is detailed, including a description of the application of the DDDAS steps. Then, predictions are considered for the cases of the C-shaped leg and the reverse C-shaped leg, from Chapters 2.2.3 and 2.2.4 respectively. Finally, a DDDAS application for the locomotion of human-sized foot on a compliant terrain is presented and discussed.

4.2.1 Description of the Case Study

The offline high-fidelity data for estimating robot appendage interaction forces are obtained from the SPH model simulations. These data are the input to the first step of the offline phase of the DDDAS, as outlined in Fig. 4.1. In this simulation, multiple inputs are incorporated to capture the nonlinear interactions between the appendage and the media, including the leg's geometry and dimensions, the granular particles' features, and the operating conditions such as the leg's angular speed ω. The outputs from the SPH model are the angles of rotation along with their corresponding horizontal and vertical forces. These results are crucial for understanding the interactions between robot appendages and their environment, which can aid the development of legged locomotion systems.

The high-fidelity datasets consist of ten simulations conducted at different angular speeds. A main objective is to examine the motion dynamics across different operating conditions. Hence, all ten datasets are derived by using the same geometric parameters—specifically, leg dimensions and granular media compaction—while varying the angular speed ω. To examine the accuracy of the DDDAS model, one out of the ten simulation datasets is set as the unseen data, comprised of the vertical F_z and horizontal F_x force values. The rest of the simulations serve as the datasets that are used in the offline phase of DDDAs for training the surrogate model.

Finally, in the context of the online phase, synthetic data are used in place of sensor observations. For an operating condition of $\omega = 0.2\,\mathrm{rad/s}$, RFT datasets generated in Chapter 2.2 are passed into the PF and assimilated into the surrogate models. This way, data assimilation can be used to improve on the prior predictions and the corresponding uncertainties are obtained from the GP regression. For the other operating conditions, since neither artificial nor experimental data are available, sensor observations are synthetically produced by a test dataset by introducing Gaussian noise to it. This also helps evaluate the impact of noise on the posterior predictions.

4.2.2 Application of DDDAS Approach for a Flat Leg

In the context of a flat leg and as part of a ten-fold cross validation method, the ten SPH simulations are separated into nine training datasets and one test dataset. During each iteration, one of the initial ten simulations serves as the test data, while the remaining simulations are fed into the model as training data. In this subsection, the application of the DDDAS framework is summarized for predicting the dynamics of a flat leg rotating at an angular speed of $0.5\,\mathrm{rad/s}$. The SPH simulation datasets and the associated operating conditions are detailed in Fig. 4.5 and Table 4.1. The test dataset under examination is indicated by black dashed curves.

Initially, the training datasets are stored in a 3D tensor $\mathcal{A} \in \mathbb{R}^{p_1 \times p_2 \times p_3}$, where p_1, p_2, and p_3 correspond to the number of the operating conditions, the time steps, and the force vector's

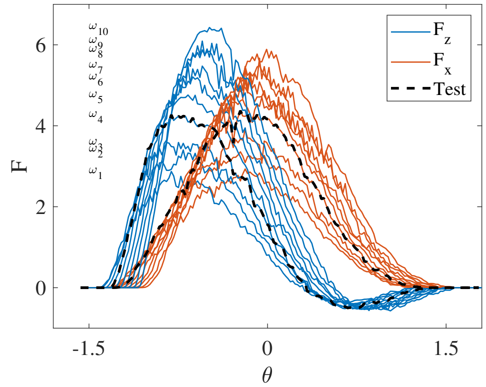

Figure 4.5: Force responses derived from high-fidelity simulations.

Table 4.1: Operating conditions used for the simulations.

Dataset	Angular Speed $\omega[rad/s]$
1	0.2
2	0.3
3	0.4
4	0.5
5	0.6
6	0.7
7	0.8
8	0.9
9	1.0
10	1.1

dimension, respectively. Tensor $\mathcal{A}$ is first decomposed into its operation and temporal-like eigen-matrices by using HOSVD. To reduce the dimensionality of the tensor while maintaining 95% of the original information, the cumulative explained variances of each singular value are studied, as illustrated in Fig. 4.6. For retaining 95% of the information, four singular values are selected for the operational dimension, and seven are chosen for the temporal-like dimension. The now truncated eigen-matrices serve as a tensor basis. By projecting the tensor $\mathcal{A}$ onto this basis, low-dimensional projected parameters are obtained for each operational condition.

As part of the second step of the offline phase, GP models are used to estimate the projected parameters for the test case involving a $0.5\,\mathrm{rad/s}$ angular speed. By integrating these parameters with the eigen-matrices derived by HOSVD, estimations of the lift and drag forces are obtained. These predictions, along with their 95% confidence interval bounds, are shown in Fig. 4.7. Having the surrogate model working with comparable accuracy provides initial predictions that subsequently become more well-informed and updated through data assimilation. Specifically, the projected parameter predictions from the GP models and their associated uncertainties serve as the prior distributions of the PF. It is assumed that N particles are drawn, each equally weighted

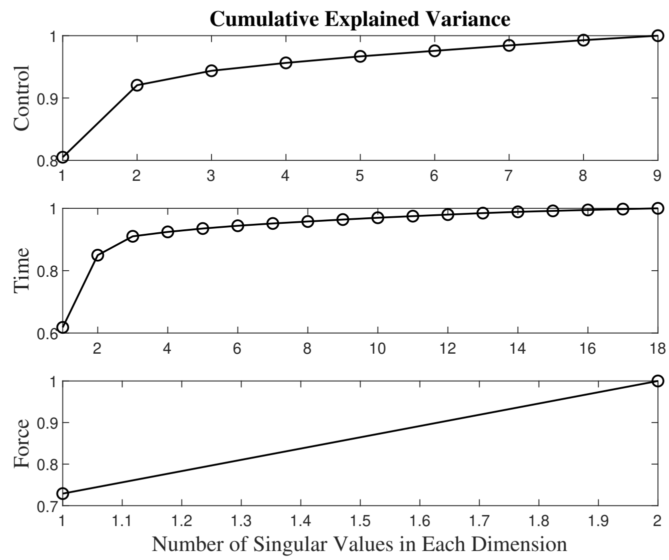

Figure 4.6: Cumulative explained variances in each dimension.

to be sampled from the prior probability density function. Given the sensor observation at the time, the probability density function is updated, leading to posterior weights for the particles. A resampling procedure ensues, ultimately resulting in a refined posterior projected parameter distribution.

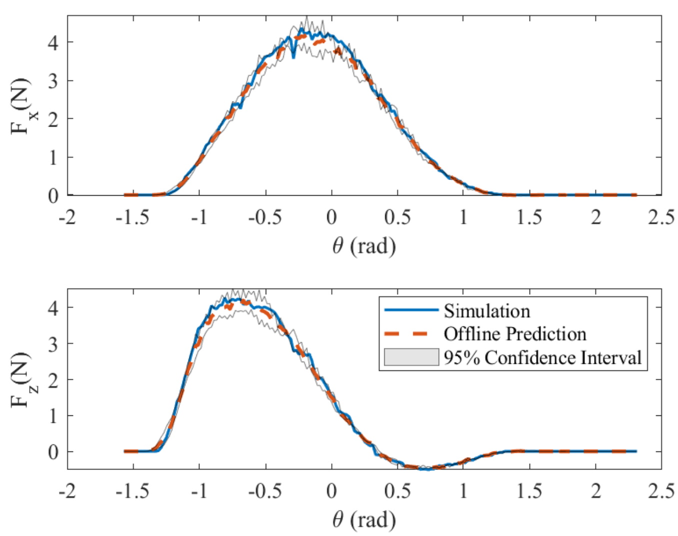

Figure 4.7: Surrogate modeling results for interactive forces between flat leg and granular media.

In Fig. 4.8, the results obtained with the DDDAS approach are shown for a flat leg for four different operating conditions. The blue solid lines represent the simulated vertical forces F_z, while the red lines correspond to the horizontal forces F_x. The scattered data marked by squares are the corresponding force predictions, which showcase a remarkable resemblance to the simulated data. This is an indication that the DDDAS is an effective way of producing accurate predictions for a variety of angular speeds.

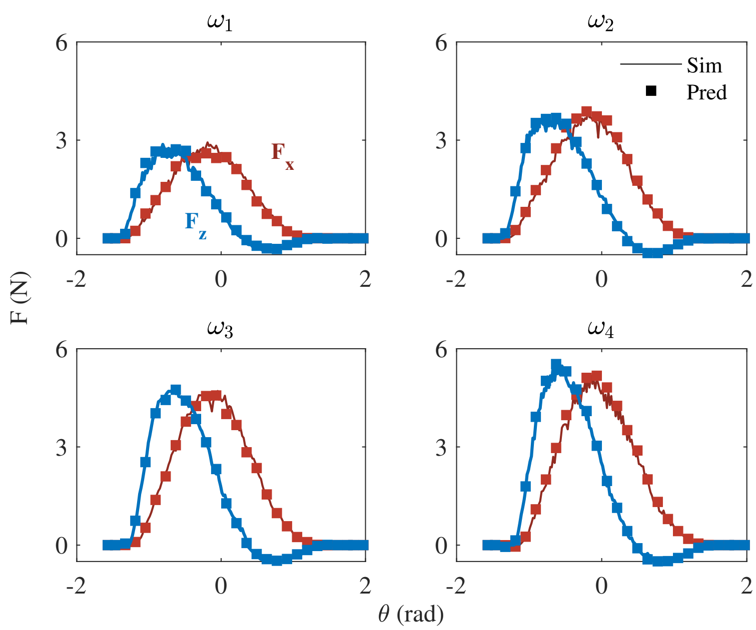

Figure 4.8: Comparison of data-driven predictions with data assimilation and physics-based simulations for flat leg.

4.2.3 DDDAS Studies for Other Leg Designs

By using the same approach, the study is extended to encompass two additional leg geometries: the C-shaped and reverse C-shaped legs. In particular, force predictions are estimated for these two leg designs with fixed geometric dimensions but varying angular speeds. The cross validation results are detailed in Fig. 4.9 and 4.10, where the blue lines correspond to the lift forces F_z and the red lines correspond to the drag forces F_x. Upon comparison with high-fidelity simulations, the predictions display a considerable level of resemblance. With both the high-fidelity simulations and the assimilated experimental measurements, the results of this study further validate the capacity of DDDAS to generate predictions of granular media interaction forces across a variety of leg geometries and operational conditions.

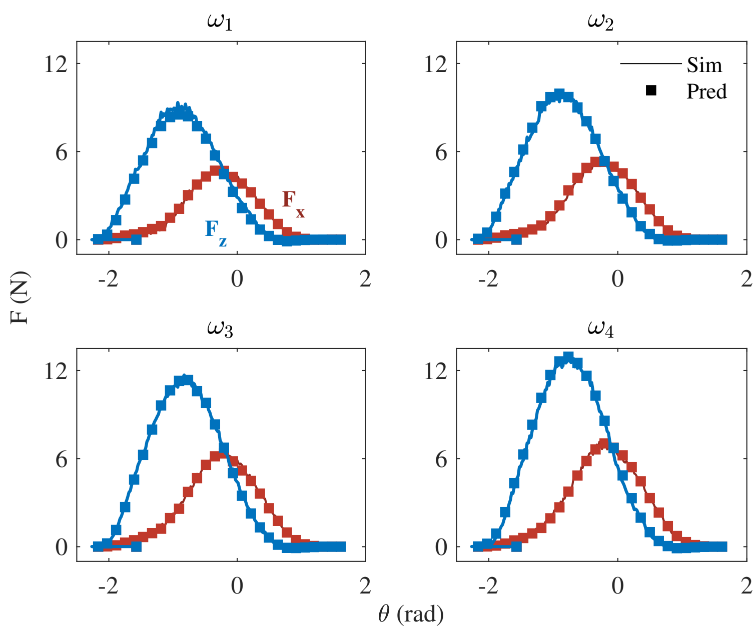

Figure 4.9: Comparison of data-driven predictions with data assimilation and physics-based simulations for C-shaped leg.

After conducting cross-validation across all available angular speeds for the three leg geometries, the MSE errors obtained between the predictions and the testing datasets are depicted in Fig. 4.11. Notably, the MSE magnitudes are consistently low, with the values well below 0.05 for the flat and reverse C-shaped leg cases, and just below 0.1 for the C-shaped leg. In comparison to the MSE errors of the predictions from the reduced-order RFT model detailed in Section 2.3, those for the DDDAS are notably smaller, especially, for the C-shaped leg case. Additionally, while the RFT model has limitations with regard to granular media type and motion speed, the

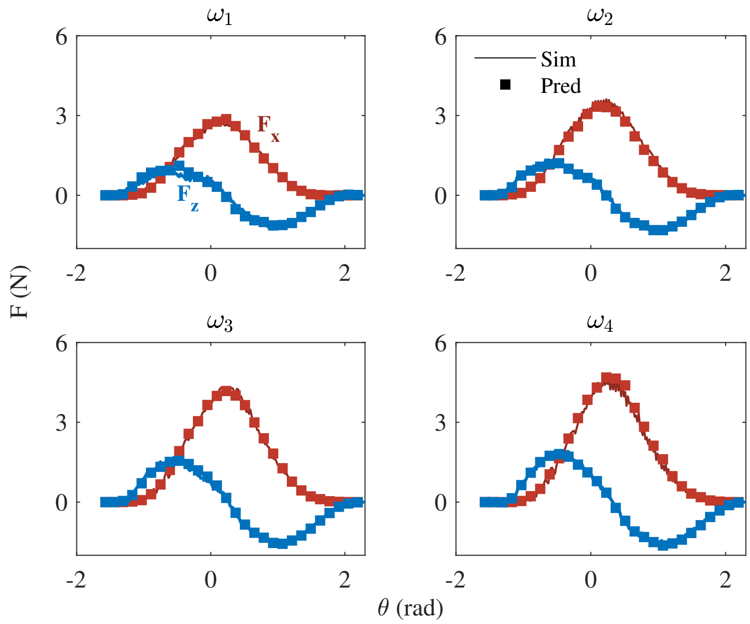

Figure 4.10: Comparison of data-driven predictions with data assimilation and physics-based simulations for reverse C-shaped leg.

DDDAS framework is noted to have greater versatility depending on the data it is fed, enabling it to capture a broader range of operational conditions.

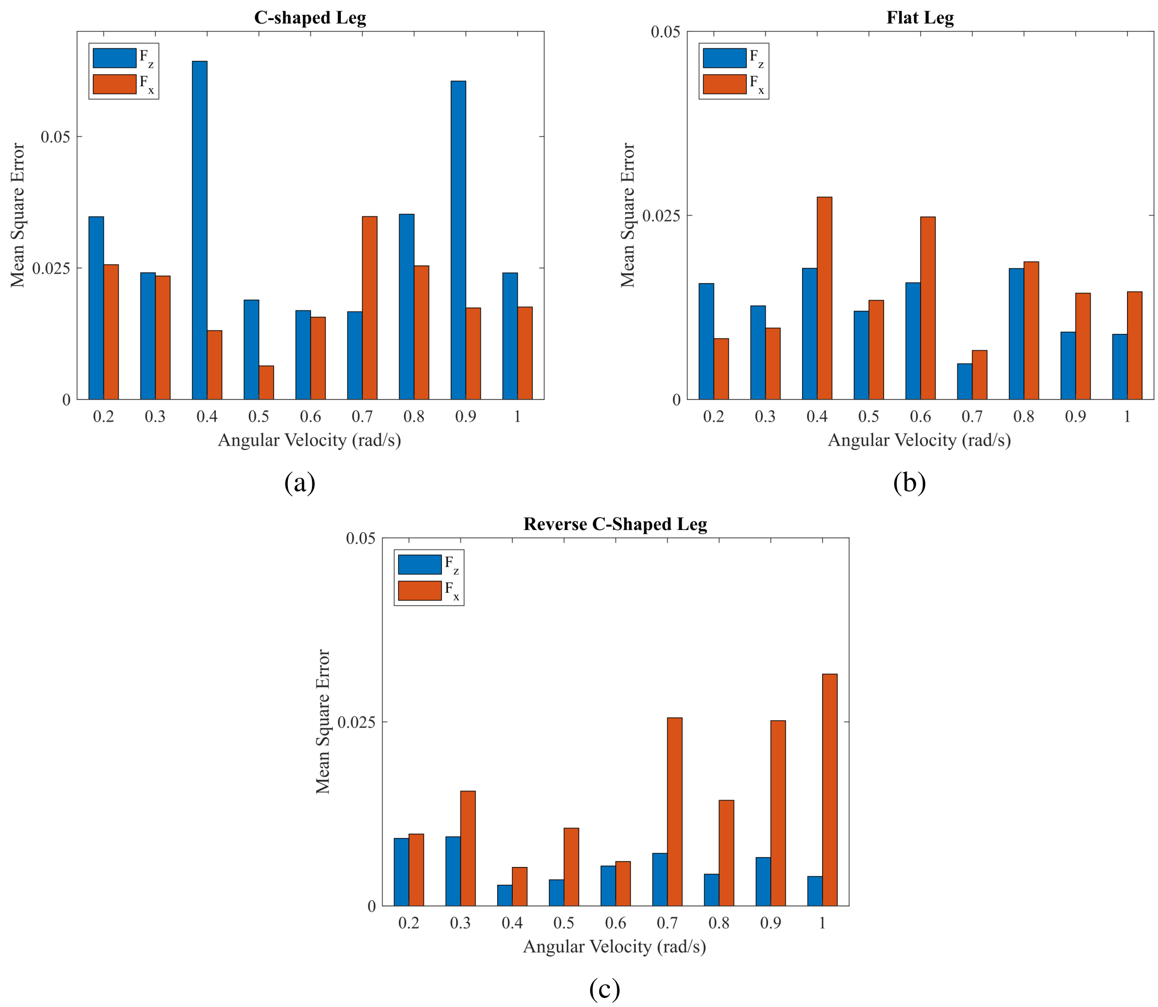

Figure 4.11: Mean Square Error for DDDAS based predictions across a variety of angular speeds for three leg geometries, a C-shaped leg, a flat leg, and a reverse C-shaped leg.

4.2.4 DDDAS Studies for Human Appendage

The DDDAS framework is finally tested on a human-sized robotic appendage. In this case study, the operational condition remains fixed while the leg's length is varied between 25.00 cm to 35.00 cm. Here, the simulation data are used as a dataset in the offline phase and this dataset is generated by using the RFT model. The results of surrogate modeling for predicting the interactive forces of a robotic appendage with a length of 29.00 cm are depicted in Fig. 4.12. In the upper subplot, both the simulation and predictions of the horizontal forces are illustrated, while the lower subplot has been made for the vertical forces. The RFT simulations are denoted by the blue solid lines, while the predictions are indicated by the red dashed lines. It is evident from the plot that the offline phase of DDDAS can produce force estimations with comparable accuracy across various leg lengths.

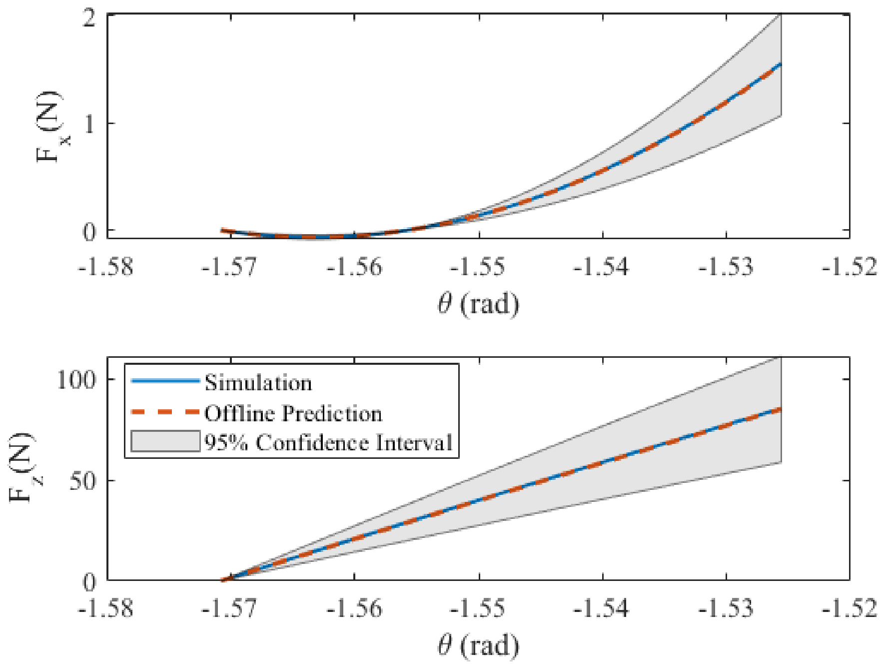

Figure 4.12: Surrogate modeling results for interactive forces between human-sized robotic appendage and granular media.

In the online phase, the available experimental data retrieved from Chapter 3, are embedded into the DDDAS framework through the PF. In Fig. 4.13, the DDDAS predictions are shown across various leg length designs, after using both RFT model based simulation data and experimental data as inputs. The solid lines correspond to the simulations, while the dashed lines represent the sensor measurements meant to help refine the predictions, which are marked by squares. Notably, compared to Fig. 4.12, in which the author has shown the force estimations for a test case without the PF, the final DDDAS predictions are significantly updated based on the

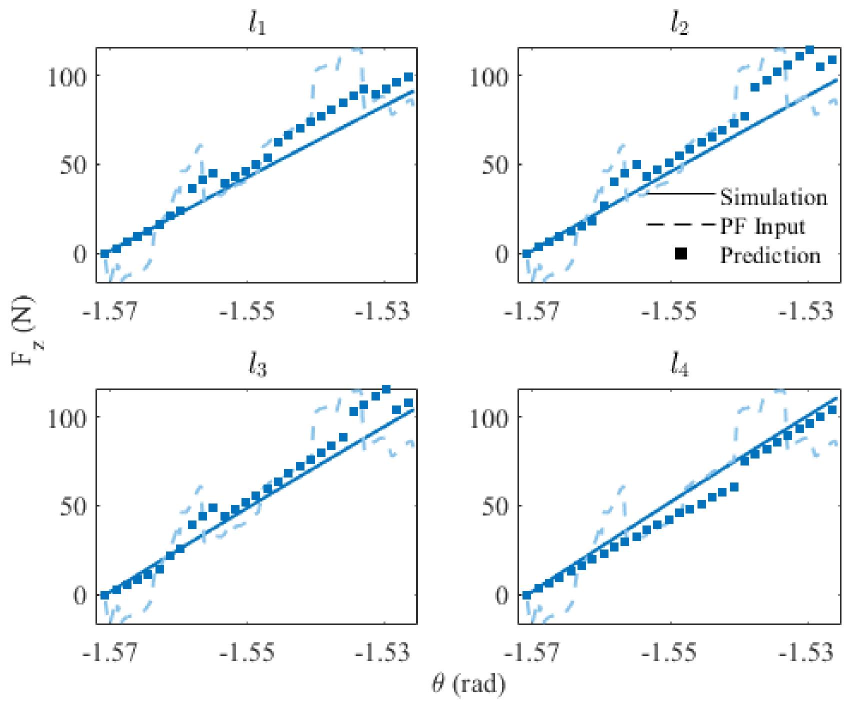

Figure 4.13: Comparison of data-driven predictions with data assimilation and physics-based simulations for human-sized robotic appendage for varying length designs.

assimilated sensor measurements. This observation suggests that predictions stemming from the combination of physics-based simulations and sensor observations can outperform high-fidelity simulations, as they tend to follow the path of the physical experimental data more closely, and also capture the transient dynamics as well.

4.2.5 Applicability of DDDAS

DDDAS is a modeling approach, in which one leverages a symbiotic relationship between simulation data and noisy sensor measurements to generate predictions under various conditions. This is especially helpful for aiding decision-making and problem-solving in unforeseeable settings in real-time. Such is the case with terrestrial locomotion, which requires a solid understanding of the physics and dynamics of interactions with deformable, compliant terrain.

As the Earth's surface is made up of a range of uneven terrains with varying compositions, it is challenging to develop a physics-based model that can quickly capture a number of events during real-time operations. Consequently, employing a data-driven approach that could be trained with accessible data across a variety of operational conditions is a viable approach for autonomous robot navigation on uneven, compliant surfaces.

The repeatability of the DDDAS framework is dependent on various factors, particularly the quality and validity of the data that is fed to the model for training. While DDDAS has been shown to have the capacity to dynamically adapt the predictions to unpredictable circumstances, the reliability and repeatability of these predictions can be undermined depending on the dataset used to form the tensor basis critical for generating the model's prior predictions offline. For instance, the composition of granular media for which the model is trained can largely differ from the terrain encountered by a robot in real-time operations. In such a case, it may be difficult for the surrogate model of the offline phase of DDDAS to accurately capture interactions that align with the ground truth. Updating the predictions with the PF by assimilating sensor measurements into the model could enhance the predictions. However, the efficiency of the approach strongly depends on the quality and sensitivity of the sensor measurements, as well as their deviation from the simulation based training datasets.

Despite its advantages, DDDAS should be used cautiously and responsibly for predictions in terrestrial locomotion. Blindly relying on the generated outcomes without prior extensive validation can result in unreliable conclusions in certain real-time operations. Focusing on a single application area can be beneficial as a starting point because the DDDAS can then be more rigorously informed and trained for a smaller scope of events. For example, in the case of a portable ankle robot such as AMBLE, which is designed for patient gait training, DDDAS could be sufficiently trained for predictions in a controlled, non-autonomous environmental setting. Once DDDAS's applicability in one application area is thoroughly tested and validated, with accompanying risk assessments, its applicability could be incrementally expanded to include more case scenarios, ensuring that it is rigorously tested for real-world applications.

Chapter 5: Conclusions and Recommendations for Future Work

5.1 Summary

In this thesis research, a reduced-order model based on the resistive forces theory (RFT) was presented and used to simulate forces that arise during locomotion on granular media. With the RFT model, one assumes that the considered granular media can exhibit both fluid-like and solid-like features. By leveraging experimental stresses per unit depth along with hydrostatic principles, the RFT model can be used to estimate the forces experienced by the numerous elements into which the leg is divided. The net forces in the horizontal and vertical direction that the leg experiences can be derived by linearly superposing the element forces.

The RFT model was used to determine the dynamic system responses for various rotating robot appendage (leg) designs in interactions with granular media. Specifically, the cases of a flat leg, a C-shaped leg, and an inverse C-shaped leg were studied. The results were subsequently validated by comparing the RFT model results to those obtained from a high-fidelity simulation model based on smoothed particle hydrodynamics (SPH) developed in earlier work in the author's group [10]. From the comparison studies, it was found that there is good consistency between the results obtained from the two models, suggesting that even though the RFT model is a reduced-order model, it is sufficient in capturing the system's responses as long as the leg is moving within the quasi-static limit; that is, when the speeds are low.

In addition, as the RFT model is reliant on experimentally extracted parameters, a variety of operational conditions can be modeled depending on the availability of data. On the other hand, the SPH model can be used to simulate various intrusion scenarios and capture the rate dependency of the system's locomotive behavior, thus enabling one to consider speeds beyond those that can be captured with the RFT model used.

Having established the two simulation models, the second part of this research was devoted to generating force predictions across a spectrum of operational conditions or leg length designs. The DDDAS framework was employed to combine data from physics-based simulations and noisy sensor measurements to produce predictions at a low computational cost. By using the DDDAS approach for various leg geometries and cross-validating across numerous angular speeds and leg lengths, it was demonstrated that the DDDAS approach based predictions have remarkable accuracy compared to the high-fidelity simulations. Additionally, the assimilation of sensor observations into the framework led to a refinement of initial surrogate modeling predictions, resulting in updates that more closely reflected real-world dynamics. This was the first such demonstration of data assimilation for an assistive robot operation.

5.2 Future Work Recommendations

Recommendations for future work include the following:

- Examine if the RFT model can be refined to be more robust in granular intrusion modeling across a variety of velocity regimes, by possibly adding an inertial correction. This will help extend the applicability of this model to higher speeds than what was done in the current work.

- Further evaluate the efficiency and robustness of both SPH and RFT based approaches, by carrying out simulations with a larger variety of leg geometries and granular materials.

- Building on the experiments reported here, conduct further experiments to collect force data, including in the horizontal direction and study assimilation of the data collected with simulation data in the DDDAS framework.

- Examine if the different components of the DDDAS approach can be better tailored for studies of robot-leg interactions with granular media.

Appendix A: Computational Code for Empirical RFT Model Based Studies in Python

In this appendix, the code developed and used for the empirical model based studies is presented.

```
import numpy as np
import pandas as pd
from scipy.interpolate import RegularGridInterpolator
import matplotlib.pyplot as plt


class StressInterpolator:
    def __init__(self, file_path):
        self.df = pd.read_excel(file_path)
        self.beta = self.get_beta()
        self.gamma = self.get_gamma()
        self.clean_dataframe()

    def clean_dataframe(self):
        self.df = self.df.drop(columns=['Unnamed: 0', 'Unnamed: 1'])
        self.df = self.df.drop(index=[0])
        self.df = self.df.set_axis([str(i) for i in range(7)], axis=0)
        self.df = self.df.set_axis([str(i) for i in range(13)], axis
           =1)

    def get_beta(self):
        beta = self.df['Unnamed: 1'][1:]
        return np.asarray(beta)

    def get_gamma(self):
        gamma = self.df.loc[0]
        gamma = np.asarray(gamma)[2:]
        return gamma.astype(float)

    def interpolate(self):
        data = np.asarray(self.df, dtype=float)
        return RegularGridInterpolator((self.beta, self.gamma), data,
           bounds_error=False, method='linear', fill_value=None)


class RFTComputation:
```

```python
def __init__(self, az_interpolator, ax_interpolator, leg_type):
    self.az_interpolator = az_interpolator
    self.ax_interpolator = ax_interpolator
    self.leg_type = leg_type

def compute_flat_leg(self, theta_range, R, d, h, n):
    lift_tot = np.empty((1, len(theta_range)), float)
    drag_tot = np.empty((1, len(theta_range)), float)

    for q, theta in enumerate(theta_range):
        lift = 0
        drag = 0
        increment = 1

        for i in range(n):
            rad = (2 * R / n) * (increment - 0.5)

            if theta <= 0:
                beta_angle = np.pi / 2 - np.abs(theta)
                gamma_angle = (np.pi / 2 - beta_angle)
                z = rad * np.sin(beta_angle)
            else:
                beta_angle = -(np.pi / 2 - theta)
                gamma_angle = -(np.pi / 2 - np.abs(beta_angle))
                z = np.abs(rad * np.sin(beta_angle))

            a_lift = self.az_interpolator((beta_angle, gamma_angle
                ))
            a_drag = self.ax_interpolator((beta_angle, gamma_angle
                ))

            if z >= h:
                sigma_z = a_lift * (z - h)
                sigma_x = a_drag * (z - h)
            else:
                sigma_z = 0
                sigma_x = 0

            increment += 1
            lift += sigma_z * (2 * R * d / n)
            drag += sigma_x * (2 * R * d / n)

        lift_tot[0, q] = lift
        drag_tot[0, q] = drag

    return lift_tot, drag_tot

def compute_c_leg(self, theta_range, R, d, h, n):
    lift_tot = np.empty((1, len(theta_range)), float)
    drag_tot = np.empty((1, len(theta_range)), float)

    for q, theta in enumerate(theta_range):
        lift = 0
        drag = 0
        increment = 0

        for i in range(n):
            if theta <= 0:
                beta_angle = increment - np.abs(theta)
```

```
                gamma_angle = -(increment / 2 - np.abs(theta))
            else:
                beta_angle = increment + theta
                gamma_angle = -(increment / 2 + theta)

            z = R * np.cos(theta) + R * np.cos(beta_angle)
            a_lift = self.az_interpolator((beta_angle, gamma_angle
               ))
            a_drag = self.ax_interpolator((beta_angle, gamma_angle
               ))

            if z >= h:
                sigma_z = a_lift * (z - h)
                sigma_x = a_drag * (z - h)
            else:
                sigma_z = 0
                sigma_x = 0

            increment += np.pi / n
            lift += sigma_z * (np.pi * R * d / n)
            drag += sigma_x * (np.pi * R * d / n)

        lift_tot[0, q] = lift
        drag_tot[0, q] = drag

    return lift_tot, drag_tot

def compute_rc_leg(self, theta_range, R, d, h, n):
    lift_tot = np.empty((1, len(theta_range)), float)
    drag_tot = np.empty((1, len(theta_range)), float)

    for q, theta in enumerate(theta_range):
        lift = 0
        drag = 0
        increment = 0

        for i in range(n):
            if theta <= 0:
                beta_angle = -(increment + np.abs(theta))
                gamma_angle = increment / 2 + np.abs(theta)
            else:
                beta_angle = -(increment - theta)
                gamma_angle = increment / 2 - theta

            z = R * np.cos(theta) + R * np.cos(np.abs(beta_angle))
            a_lift = self.az_interpolator((beta_angle, gamma_angle
               ))
            a_drag = self.ax_interpolator((beta_angle, gamma_angle
               ))

            if z >= h:
                sigma_z = a_lift * (z - h)
                sigma_x = a_drag * (z - h)
            else:
                sigma_z = 0
                sigma_x = 0

            increment += np.pi / n
            lift += sigma_z * (np.pi * R * d / n)
```

```
                drag += sigma_x * (np.pi * R * d / n)

            lift_tot[0, q] = lift
            drag_tot[0, q] = drag

        return lift_tot, drag_tot

    def compute_rft(self, theta_range, R, d, h, n):
        if self.leg_type == 'flat':
            return self.compute_flat_leg(theta_range, R, d, h, n)
        elif self.leg_type == 'c-shaped':
            return self.compute_c_leg(theta_range, R, d, h, n)
        elif self.leg_type == 'rev-c-shaped':
            return self.compute_rc_leg(theta_range, R, d, h, n)
        else:
            raise ValueError("Invalid leg type. Choose 'flat' or 'c-
               shaped'.")


# Load data
az_interpolator = StressInterpolator(r'C:\Users\chris\PycharmProjects\
   pythonProject\az_poppy_lp.xlsx').interpolate()
ax_interpolator = StressInterpolator(r'C:\Users\chris\PycharmProjects\
   pythonProject\ax_poppy_lp.xlsx').interpolate()

# RFT Computation
R = 7.62 / 2  # Radius of leg [cm]
d = 2.54      # Width of leg [cm]
h = 2         # Hip height [cm]
n = 100       # number of leg elements
theta_range = np.linspace(-2.35619, 2.35619, 200)

rft_comp = RFTComputation(az_interpolator, ax_interpolator, 'rev-c-
   shaped')
lift_tot, drag_tot = rft_comp.compute_rft(theta_range, R, d, h, n)

# Plotting
plt.figure()
plt.plot(theta_range, lift_tot[0], label='Lift')
plt.plot(theta_range, drag_tot[0], label='Drag')
plt.xlabel('Angle (theta)')
plt.ylabel('Force')
plt.title('Lift and Drag vs. Angle')
plt.legend()
plt.show()
```

Bibliography

[1] A. Nikolakakis, I. Kontolatis, N. Cherouvim, P. Chatzakos, and E. Papadopoulos. Implementation of a quadruped robot pronking/bounding gait using a multipart controller. 2, 01 2010.

[2] M. G. Bekker. *Off-the-road locomotion; research and development in terramechanics.* University of Michigan Press, Ann Arbor, 1960.

[3] A. Mehta. Spatial, dynamical and spatiotemporal heterogeneities in granular media. *Soft Matter*, 6, 07 2010.

[4] S. Agarwal, A. Karsai, D. I. Goldman, and K. Kamrin. Surprising simplicity in the modeling of dynamic granular intrusion. *Science advances*, 7, 04 2021.

[5] R. Maladen, Y. Ding, P. Umbanhowar, A. Kamor, and D. I. Goldman. Mechanical models of sandfish locomotion reveal principles of high performance subsurface sand-swimming. *Journal of the Royal Society, Interface / the Royal Society*, 8:1332–45, 03 2011.

[6] F. Qian, T. Zhang, C. Li, P. Masarati, A. M. Hoover, P. Birkmeyer, A. Pullin, R. S. Fearing, and D. I. Goldman. Walking and Running on Yielding and Fluidizing Ground. In *Robotics: Science and Systems VIII*. The MIT Press, 07 2013.

[7] P. Ravula. *Numerical and experimental studies on dynamic interactions of robot appendages with granular media*. Ph.D. Dissertation, University of Maryland, 2021.

[8] G. Dilber Acar, P. Ravula, and B. Balachandran. Dynamic interactions of a driven pendulum with photoelastic granular media. *Physics Letters A*, 396:127244, 2021.

[9] P. Ravula, G. Acar, and B. Balachandran. Discrete element method-based studies on dynamic interactions of a lugged wheel with granular media. *Journal of Terramechanics*, 94:49–62, 2021.

[10] G. Wang, A. Riaz, and B. Balachandran. Continuum modeling and simulation of robotic appendage interaction with granular material. *Journal of Applied Mechanics*, 88, 11 2020.

[11] C. Li, T. Zhang, and D. I. Goldman. A terradynamics of legged locomotion on granular media. *Science*, 339(6126):1408–1412, 2013.

[12] G. Wang, A. Riaz, and B. Balachandran. Computational studies on interactions between robot leg and deformable terrain. *Procedia Engineering*, 199:2439–2444, 2017. X International Conference on Structural Dynamics, EURODYN 2017.

[13] C. Li, T. Zhang, and D. I. Goldman. A resistive force model of legged locomotion on granular media. 10 2019.

[14] F. Darema. Dynamic data driven applications systems: A new paradigm for application simulations and measurements. In M. Bubak, G. D. van Albada, P. M. A. Sloot, and J. Dongarra, editors, *Computational Science - ICCS 2004*, pages 662–669, Berlin, Heidelberg, 2004. Springer Berlin Heidelberg.

[15] X. Zhao, A. Kebbie-Anthony, S. Azarm, and B. Balachandran. Dynamic data-driven multi-step-ahead prediction with simulation data and sensor measurements. *AIAA Journal*, 57(6):2270–2279, 2019.

[16] X. Zhao, S. Azarm, and B. Balachandran. Dynamic data-driven spatiotemporal system behavior prediction with simulations and sensor measurement data. page V02BT03A060, 08 2018.

[17] G. Wang. *Physics-based and data-driven modeling of hybrid robot movement on soft terrain*. Ph.D. Dissertation, University of Maryland, 2020.

[18] H. H. Bui, R. Fukagawa, K. Sako, and S. Ohno. Lagrangian meshfree particles method (sph) for large deformation and failure flows of geomaterial using elastic–plastic soil constitutive model. *International Journal for Numerical and Analytical Methods in Geomechanics*, 32(12):1537–1570, 2008.

[19] G. R. Liu and M. B. Liu. *Smoothed Particle Hydrodynamics*. WORLD SCIENTIFIC, 2003.

[20] R. G. Cox. The motion of long slender bodies in a viscous fluid part 1. general theory. *Journal of Fluid Mechanics*, 44(4):791–810, 1970.

[21] T. Zhang and D. I. Goldman. The effectiveness of resistive force theory in granular locomotion. *Physics of Fluids*, 26(10):101308, 10 2014.

[22] C. Li, Y. Ding, N. Gravish, R. D. Maladen, A. Masse, P. B. Umbanhowar, H. Komsuoglu, D. E. Koditschek, and D. I. Goldman. *Toward a Terramechanics for Bio-Inspired Locomotion in Granular Environments*, pages 264–273.

[23] X. Zhao. *Data-driven prediction, design, and control of system behavior using statistical learning*. Ph.D. Dissertation, University of Maryland, 2021.

[24] S. Yi and J. Song. Particle filter based monitoring and prediction of spatiotemporal corrosion using successive measurements of structural responses. *Sensors*, 18(11), 2018.